Bulletin of Earthquake Engineering (2022) 20:3385–3441
https://doi.org/10.1007/s10518-022-01384-1

S.I. : SOIL-STRUCTURE INTERACTION EFFECTS ON THE DYNAMICS OF STRUCTURES

Seismic resilience of extra-large LNG tank built on liquefiable soil deposit capturing soil-pile-structure interaction

Noor Sharari[1] · Behzad Fatahi[2] · Aslan Hokmabadi[3] · Ruoshi Xu[4]

Received: 31 July 2021 / Accepted: 8 March 2022 / Published online: 23 April 2022

Abstract
Assessment of seismic resilience of critical infrastructure such as liquefied natural gas (LNG) storage tanks, is essential to ensure availability and security of services during and after occurrence of large earthquakes. In many projects, it is preferred to build energy storage facilities in coastal areas for the ease of sea transportation, where weak soils such as soft clay and loose sand with liquefaction potential may be present. In this study, three-dimensional finite element model is implemented to examine the seismic response of a 160,000 m^3 full containment LNG tank supported by 289 reinforced concrete piles constructed on liquefiable soil overlaying the soft clay deposit. The seismic soil-structure interaction analysis was conducted through direct method in the time domain subjected to the 1999 Chi-Chi and the 1968 Hachinohe earthquakes, scaled to Safe Shutdown Earthquake hazard level for design of LNG tanks. The analyses considered different thicknesses of the liquified soil deposit varying from zero (no liquefaction) to 15 m measured from the ground surface. The key design parameters inspected for the LNG tank include the acceleration profile for both inner and outer tanks, the axial, hoop and shear forces as well as the von Mises stresses in the inner tank wall containing the LNG, in addition to the pile response in terms of lateral displacements, shear forces and bending moments. The results show that the seismic forces generated in the superstructure decreased with increasing the liquefied soil depth. In particular, the von Mises stresses in the inner steel tank exceeded the yield stress for non-liquefied soil deposit, and the elastic–plastic buckling was initiated in the upper section of the tank where plastic deformations were detected as a result of excessive von Mises stresses. However, when soil liquefaction occurred, although von Mises stresses in the inner tank shell remained below the yield limit, localised stress concentrations were observed in the lower section of the tank near the base, increasing the risk of the elephant foot buckling. The lateral displacements, shear forces and bending moments in the piles increased with increasing depth of the liquefied soil. Indeed, increasing the pile lateral displacement amplified the bending moment at the pile head, thus resulting in increases in the pile bending moments especially when the liquefied soil depth exceeded one third of the entire soil deposit. In particular, the bending moment at the pile head exceeded the yield moment capacity of the pile and subsequent plastic hinges were formed. Moreover, when the thickness of the liquefied soil was more than half of the entire soil depth, the mobilised

Extended author information available on the last page of the article

bending moments in the piles exceed the ultimate moment capacity of the pile and thus total failure of the piles were observed. In addition, in the absence of liquefied soil layer, the inertial interaction had a dominant impact on the pile response in this study. However, with increasing the thickness of the liquefied layer, further loads were developed in the piles due to amplified kinematic interaction, while the inertial interaction-induced loads decreased.

Keywords Seismic design · Soil-structure interaction · LNG tank · Piles · ABAQUS · Numerical modelling

List of symbols

$\langle \cdot \rangle$	Macaulay bracket
$\Delta \boldsymbol{h}$	Small height segment of tank wall
α	Back stress
α^{dev}	Devatoric part of back stress tensor
α^{s}	Back stress at large plastic strains
$\alpha_{damping}$	Rayleigh coefficients viscous damping
$\boldsymbol{A_g(t)}$	Horizontal ground acceleration
$\beta_{damping}$	Rayleigh coefficients viscous damping
γ_k	Hardening modulus decreasing rate
γ_{ref}	Refernce shear strain
γ	Cyclic shear strain
γl	Non-diamntional factor
ρ	Fluid density
ρ_{soil}	Soil density
ρ_c	Concrete density
ρ_r	Steel rebar density
ρ_{steel}	Ni steel desity
C_{con}	Sloshing period coefficient
$C_{h(T)}$	Spectral shape factor
C_{imp}	Impulsive pressure distribution coefficient
C_k	Initial kinematic hardening modulus
$\boldsymbol{C_I}$	Coefficient of impulsive period
$\boldsymbol{c_p}$	Dilatational (pressure) speed
CS	Kinematic hardening modulus for steel
$\boldsymbol{c_{sv}}$	Shear wave speeds
C_u	Undrained shear strength
D	Tank diameter
D_k	Building damping ratio
dt	Tensile damage parameter
dc	Compressive damage parameter
E_0	Intial elastic stiffness
Ec	Young's modulus of elasticity of concreter
Er	Young's modulus of elasticity of rebar
Es	Young's modulus of elasticity of 9% Ni steel
h	Overclosure
H	Tank height
H_{con}	Convective mass height

H_L	Fluid design level
F	Yield surface function
$f(\sigma-\alpha)$	Equivelant Mises stress
f_{bo}	Biaxial compressive yield strengths
f_{co}	Uniaxial compressive yield strengths
f_{ult}	Ultimate tensile strength
f_y	Tensile yield stress
f_c'	Concrete compressive strength
G/G_{max}	Modulus reduction ratio
G_{max}	Maximum shearmodulus
G_{sec}	Secant shear modulus
I_1', I_1	Modified Bessel functions of order 1 and its derivative
I_g	Reduction factor modulus
K_c	Tensile to the compressive meridian ratio
I_{con}	Convective mode spring stifness
N_{max}	Coffiecient for fualt distance
$(N_1)_{60cs-Sr}$	Equivalent SPT value
M_{con}	Covective mass
m_{imp}	Implusive mass
P	Contact pressure
p_{imp}	Hydrodynamic pressure
$\bar{p}$	Hydrostatic stress
$\bar{q}$	Von Mises effective stress
Q	Flow potential function
R	Return period factor
R^2	Coefficient of determination
R_{tank}	Tank radiuos
r	Cylindrical coordinates of tank
S	Deviatoric stress tensor
S_r	Residual shear strength
t	Time
T	Structure period
T_{imp}	Impulsive natural period
T_{con}	Convective natural period
t_u	Equivalent uniform thickness of the tank wall
V_s	Shear wave velocity
Z	Hazard factor
z	Cylindrical coordinates of tank
δ	Elongation
$\dot{\bar{\varepsilon}}^{pl}$	Equivalent plastic strain rate
$\bar{\varepsilon}_c^{in}$	Inelastic crushing strain
$\bar{\varepsilon}_c^{pl}$	Compressive plastic strain
$\bar{\varepsilon}_t^{cr}$	Cracking strain
$\bar{\varepsilon}_t^{pl}$	Tensile plastic strain
$\dot{\varepsilon}^{pl}$	Plastic flow rate
ε_t^{pl}	Tensile plastic strain
$\in$	Eccentricity of plastic potential surface
ε_c	Compressive strain
ε_{eng}	Nominal strain values

ε_t	Tensile strain
ε_{true}	True (logarithmic) strain
v	Poisson's Ratio
ξ	Non-dimensional coordinates
$\xi_{damping}$	Soil damping
ξ_{max}	Maximum damping ratio
ς	Non-dimensional coordinates
$\bar{\sigma}_{max}$	Maximum principal effective stress
$\bar{\sigma}_c$	Effective compressive stress
$\bar{\sigma}_t$	Effective tension stress
σ_c	Compression stress
σ_{eng}	Nominal stress- strain values
σ_t	Tensile stress
σ_{t0}	Tensile stress at failure
σ_{true}	Cauchy stress
σ_{ult}	Ultimate stress
σ_{vc}	Effective vertical stress
σ_y	Yield stress
$\sigma\|_0$	Initial yield stress
τ	The shear stress
$\tau_{critical}$	Critical contact shear stress
τ_{rev}	Shear stress at the reversal point
ψ	The dilation angle
φ	Soil friction angle
μ	Friction coefficient
θ	Cylindrical coordinates of tank

1 Introduction

Liquid storage tanks have always been an important link in the distribution of water, chemical and refined petroleum products. In particular, during the past 30 years, the demand on the Liquefied Natural Gas (LNG) tanks has increase significantly (Animah and Shafiee 2020). As the LNG is cleaner and a cheaper fuel for power generation than oil and coal, it is considered as a transition and rather environmentally friendly energy fossil fuel source. While large water storage tanks located near cities and populated areas are in demand to ensure constant water supply, oil and liquefied natural gas storage tanks are generally located in refineries, terminals and ports to reduce the transportation cost and stay away from populated areas for safety reasons (Solakivi et al. 2019).

Indeed, natural gas is primarily made of methane, and to reduce the storage space, it is liquefied and stored at atmospheric pressures while operating at temperatures around − 166 °C. LNG tanks are usually built in areas near the shorelines to increase the flexibility of LNG transportation and reduce the traveling and storage cost. These tanks have capacities ranging from 160,000 to 225,000 m^3 corresponding to diameters of 80 m to 100 m and heights from 30 to 50 m (Nagashima et al. 2011; Calderón et al. 2016). Thus, the foundation soil may not be capable of bearing the load of such heavy structure, and usually deep foundations are used to support these tanks built on weak soils near ports. Pile foundations are commonly used to support these types of extra-large tanks to carry

the entire load and control the settlement (Hor et al. 2017). Indeed, when utilising the pile foundation, the LNG tank load is transferred to the piles through rigid reinforced slab at the base of the tank, which acts as a load distribution mat.

The LNG industry is growing quickly and many LNG tanks are constructed in seismically active coastal regions; hence, potential damage or leak due to cracking triggered by earthquake can result in the catastrophic environmental and safety threatening events (Zhang et al. 2011; Zhai et al. 2019). The LNG tanks should be designed wisely for safe and secure energy storage, and to meet the stringent requirements, the liquid inside the tank is usually contained within a steel container with high ductility material to ensure high performance subjected to low temperatures. Researchers have found that the inner container performance could be enhanced by using 9% nickel steel inner tank, surrounded by insulation materials (Chung et al. 2019). Moreover, for external protection and vapour containment, prestressed concrete outer tanks are usually used (Zhai et al. 2019). This type of tank, with inner steel tank and outer concrete tank with insulation material in between, is known as full containment tank, which is the most commonly used tank in practice to store LNG.

The seismic performance of LNG storage tanks has been a matter of special importance, beyond the economic value of the structure, due to the requirement to remain functional after a major earthquake event (Di Sarno 2020). Any potential danger associated with the failure of tanks containing highly flammable products can lead to extensive uncontrolled fires while any possible spillage of such content might cause extensive environmental damage and affect populated areas (Zhang et al. 2018). Therefore, the need for quite advanced experimental, analytical and numerical investigations to assess the seismic response of such structures, is quite evident.

Under earthquake loading, the dynamic behaviour of LNG tank is quite complicated due to Soil-Structure Interaction (SSI) and Fluid–Structure Interaction (FSI) effects. Under dynamic loading, the LNG exerts additional hydrodynamic forces on to the tank walls. These hydrodynamic forces have two components; in the first component, portion of the liquid is accelerated with the tank walls and acts as added mass (or impulsive force), while in the second component, the upper portion of liquid sloshes generating surface waves (i.e. convective force), and the characteristics of these waves are affected by ground displacement rather than ground acceleration (Christovasilis and Whittaker 2008). Many researchers studied the FSI effects on liquid storage tanks under dynamic loading (e.g. Housner 1957; Veletsos and Tang 1987; Haroun and Housner 1981; Malhotra et al. 2000) and proposed a simple mechanical model to capture the FSI, where the two hydrodynamic forces can be represented by concentrated forces attached to the tank wall with appropriate links. Indeed, the simplified analytical models are adopted in several well-established design codes such as API 650 (2007) and NZSEE (2009). Later, Virella et al. (2006) enhanced the simplified mechanical models to capture FSI by replacing the hydrodynamic concentrated forces with distributed forces along the tank wall as adopted in Eurocode (2008).

Evidently, the SSI could greatly alert the dynamic behaviour of the superstructures and their supporting foundation system, and indeed the contribution of SSI is significantly increased when the superstructure is constructed on soft soil deposits in seismically active areas (Gazetas and Mylonakis 1998; Stewart et al. 2000; Mylonakis and Gazetas 2000; Trifunac 2000; Carbonari et al. 2008; Padrón et al. 2009; Gičev and Trifunac 2012; Hokmabadi and Fatahi 2016; Asimaki et al. 2019; Elwardany et al. 2019; Cavalieri et al. 2020; Brunelli et al. 2021). Medina et al. (2013) assessed the SSI effects on seismic characteristics of pile supported structures including period of vibration and damping implementing substructure analysis method. The results highlighted the importance of pile characteristics

on the response of both high and short buildings. Zimmaro and Ausilio (2020) investigated the dynamic properties and seismic behaviour of earth fill dam foundations using modal and seismic hazard analyses, and showed that the substantial underestimation of the fundamental period of the dam could be observed when the SSI effects was ignored.

Similarly, since the SSI can significantly affect the seismic response of large capacity structures like LNG tanks, several researchers investigate SSI effects on the seismic response of LNG tanks (Willford et al. 2010; Ruiz and Gutiérrez 2015; Tajirian et al. 2019). For example, Sun and Cui (2015) studied the seismic response of the base-isolated LNG tank taking into account the SSI effect using a simplified mechanical model and elastic soil foundation. Their results illustrtaed the importance of SSI on selecting the best isolation system. Son and Kim (2019) highlighted the importance of SSI effects on the seismic response of LNG tank subjected to vertical earthquake component. Moreover, Hokmabadi et al. (2019) considered the impact of SSI on the seismic response of a large LNG tank sitting on the improved ground, and highlighted the importance of conducting rigorous numerical modelling to optimise the seismic design of LNG tanks.

One of the most dramatic causes of damage to structures during earthquakes is the occurrence of liquefaction in saturated sand deposits. Loose sand tends to contract under the cyclic loading imposed by earthquake shaking, which can cause increase in excess pore water pressure if the soil is saturated and unable to drain during earthquake. This results in reduction in soil effective stress and consequently substantial loss of soil strength and stiffness (Booth and Fenwick 1994; Bhattacharya and Madabhushi 2008). Several infrastructures and buildings suffered severe damages from soil liquefaction in the past earthquakes such as the 1964 Niigata, the 1971 San Fernando, the 1989 Loma Prieta and the 1995 Kobe earthquakes (Abdoun and Dobry 2002; Brandenberg et al. 2018; Jiménez et al. 2019; Zimmaro et al. 2020).

The liquefaction hazard should be evaluated in the seismic design of the projects. This includes undertaking liquefaction assessment to identify layers with liquefaction potential under the design earthquakes. The consequences of onset of potential liquefaction should be assessed and addressed in the design. From authors design experience, ground improvement techniques (e.g. deep cement mixing, jet grouting, stone columns) or pile foundations are common solutions to mitigate the liquefaction hazard in the design of large LNG tanks. While ground improvement techniques are considered to be more economical in many cases, their application depends on site ground conditions, extent of the liquefiable hazard, and project specific requirements. On the other hand, pile foundations offer a robust solution for the design of large LNG tanks and have been adopted in many projects.

The seismic response of large LNG tanks founded on potentially liquefiable soil needs a precise consideration of soil-pile-structure interaction. This is not only required for the design of pile elements, but the impact of soil liquefaction on the overall response of the LNG tanks is crucial and should be well understood. Many studies had highlighted the potential failure of pile foundation in liquefiable soils due to buckling instability, bending, shear or settlement failures of piles during earthquakes (e.g. Tokimatsu et al. 1996; Dash et al. 2009; Haldar and Babu 2010; Zhuang et al. 2015). However, there is very limited research available in the literature on the response of LNG tanks founded on pile foundation in potentially liquefiable soil deposits. Thus, in this study, the effect of the depth of liquefied soil deposit on the seismic response of LNG tank supported by pile foundation will be examined using three-dimensional finite element analysis. Results of this study can be used to assess the seismic efficiency of end-bearing pile foundation to support extra-large LNG tanks on liquefiable soils without ground improvement.

2 Overview of adopted LNG tank and soil profile

In this study, a 160,000 m^3 full containment LNG tank is used to perform the seismic analysis. The adopted LNG tank is an example of extra-large tank constructed in highly to moderately seismic regions. This tank consists of an open top 9% Ni steel inner tank and an outer reinforced concrete (RC) tank with fixed roof, sitting on end-bearing pile raft foundation system. Figure 1 shows the overview of the structural and geometrical features of the adopted LNG tank. The total height of the outer RC tank is 51.20 m, the outer tank wall is 42.27 m high, the inner tank wall is 40.0 m high and the LNG design level in the inner tank is 36.0 m. The inner 9% Ni steel tank wall thickness is varying from 40.0 mm (bottom) to 10.0 mm (top), and the outer tank wall thickness is 800 mm. Figure 1b illustrates the layout of 289 reinforce concrete piles, while Fig. 1c shows the details of the piles supporting the raft foundation (i.e. tank slab).

Figure 2 shows the adopted soil profiles in this study to assess the impacts of depth of liquefiable soil on the seismic response of the LNG tanks. Figure 2a shows the adopted benchmark scenario in which the LNG tank sitting on soft clay soil deposit (non-liquefiable) with the average shear wave velocity $V_s = 225$ m/s for the top 15.0 m of soil deposit, and $V_s = 270$ m/s from 15.0 to 30.0 m depth. This benchmark subsoil profile (Scenario I) is classified as site Class *C* (Soft Soil Site) according to AS/NZS1170.4 (2004). It should be note that it is assumed that the soil deposit is underlain by Sandstone rock with shear wave velocity in excess of 760 m/s and the unconfined compressive strength greater than 50 MPa. To assess impacts of presence of liquefiable soil deposit on the seismic response of LNG tank system, three other scenarios with different depths of liquefiable soil are considered as in Fig. 2, namely Scenario II (5 m deep liquefiable soil), Scenario III (10 m deep liquefiable soil) and Scenario IV (15 m liquefiable soil). Further details about adopted properties of the liquefied soil deposits are provided in the next section.

3 Details of numerical modelling

In this study, the three dimensional finite element analysis was conducted using ABAQUS (2018) software, where the superstructure, pile foundation and the soil were simulated using fully nonlinear direct method (Kramer 1996), where the LNG tank, foundation and the soil were treated with the same rigour. Taking the advantage of the fact that the problem is symmetric about the line of symmetry parallel to the direction of the applied earthquake, only half of the model was simulated in this study as shown in Fig. 3.

3.1 Modelling of the inner and outer tanks and pile foundation

The inner 9% Ni steel and outer reinforced (RC) concrete tanks were modelled using S4R shell elements. Additionally, the steel reinforcements in the RC tank wall, roof and slab were modelled as uniaxial reinforcement layers embedded in the shell element, similar to the technique used by other researchers to simulate axial and circumferential steel rebars (e.g. Nateghi and Yakhchalian 2011; Hafez 2012; Zhai et al. 2019).

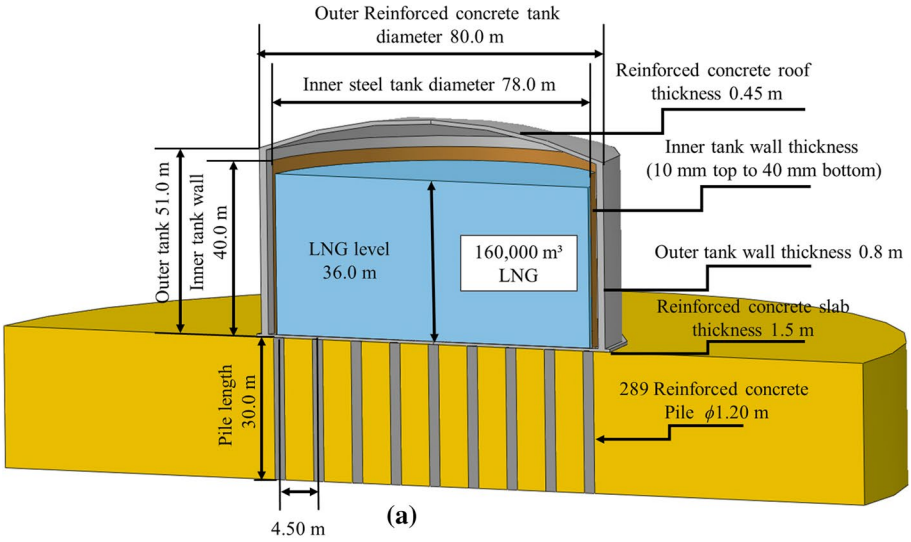

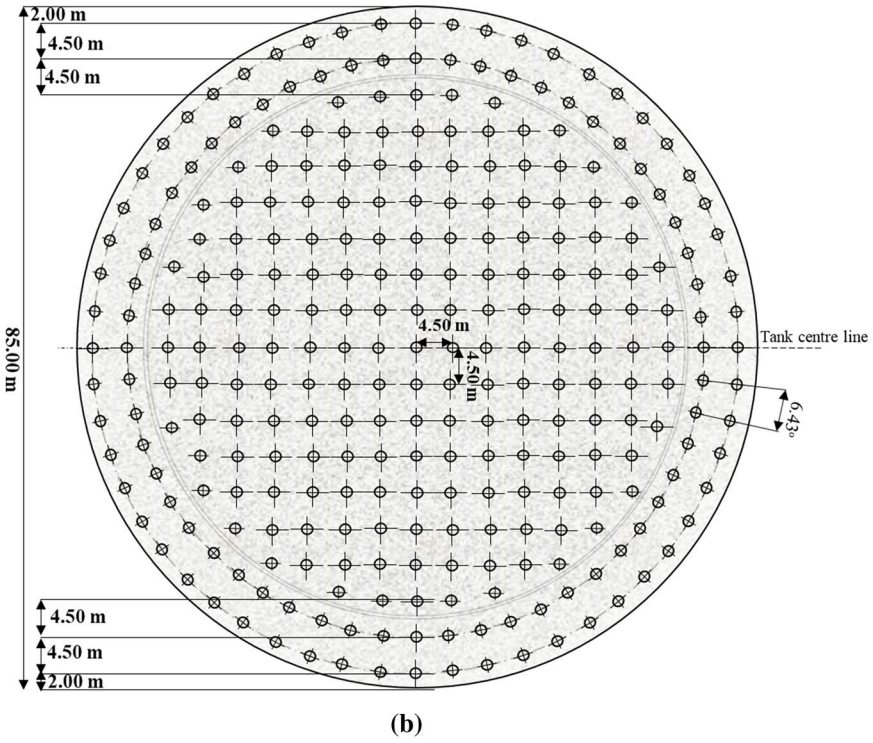

Fig. 1 The LNG tank adopted in this study **a** LNG tank configuration including the superstructure and foundation details; **b** the plan view of the arrangement 289 piles supporting the LNG tank and **c** end bearing pile details

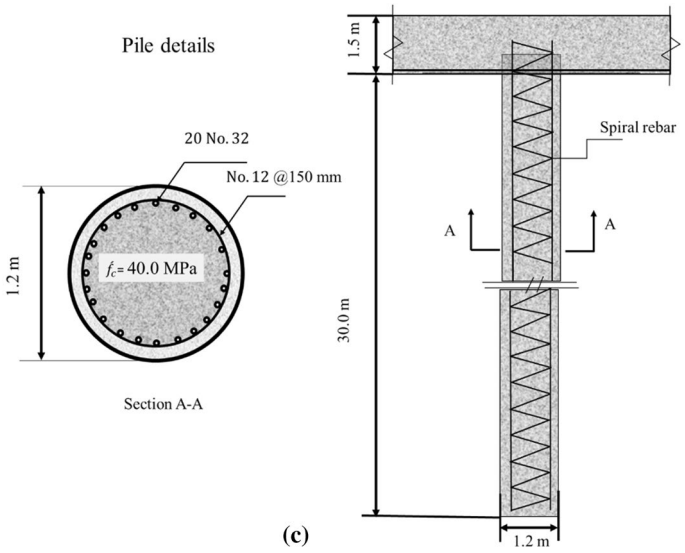

Fig. 1 (continued)

3.1.1 Modelling of outer reinforced concrete tank

The concrete damage plasticity (CDP) model was implemented in this study to model the outer concrete containment of LNG tank under the seismic loading. As explained by several researchers (Zhai et al. 2019; Hafez 2012; Dulinska and Jasinska 2014), this model is suitable to capture the concrete behaviour under dynamic loading particularly for thin wall structures such as concrete tanks and pipes. Indeed, this model adopts plasticity-based damage for the concrete, assuming two failure mechanisms, namely the tensile cracking and compressive crushing to represent the inelastic behaviour of concrete. The evolution of yield surfaces was controlled by two hardening variables, namely the tensile plastic strain ($\overline{\varepsilon}_t^{pl}$), and the compressive plastic strain ($\overline{\varepsilon}_c^{pl}$). where f_{b0} and f_{c0} are the biaxial and uniaxial compressive yield strengths, respectively. Moreover, $\tilde{\sigma}_c$ and $\tilde{\sigma}_t$ are the effective compressive and tensile stresses respectively (i.e. the stresses determined based on undamaged elastic stiffness). K_c is the ratio of the second stress invariants on tensile and compressive meridians, which defines the shape of the yield surface. Since the CDP model adopts non-associated flow rule proposed by Lee and Fenves (1998), the yield surface differs from the potential plastic flow, which utilises the Drucker-Prager hyperbolic function to formulate the flow potential function Q as follows:

$$Q = \sqrt{(\in \sigma_{t0} \tan\psi)^2 + \overline{q}^2} - \overline{p} \tan\psi \tag{1}$$

where σ_{t0} is the tensile stress at failure (i.e. tensile strength), ϵ is the eccentricity of plastic potential surface, and ψ is the dilation angle measured in $\overline{q} - \overline{p}$ space.

The degradation of concrete strength and stiffness in this adopted CDP model is captured via tension and compression damage parameters (d_t and d_c), where these model parameters refer to the weakened concrete characteristics during unloading response as a result of cracking and crushing impacting the initial elastic stiffness (i.e. E_0). Indeed, the

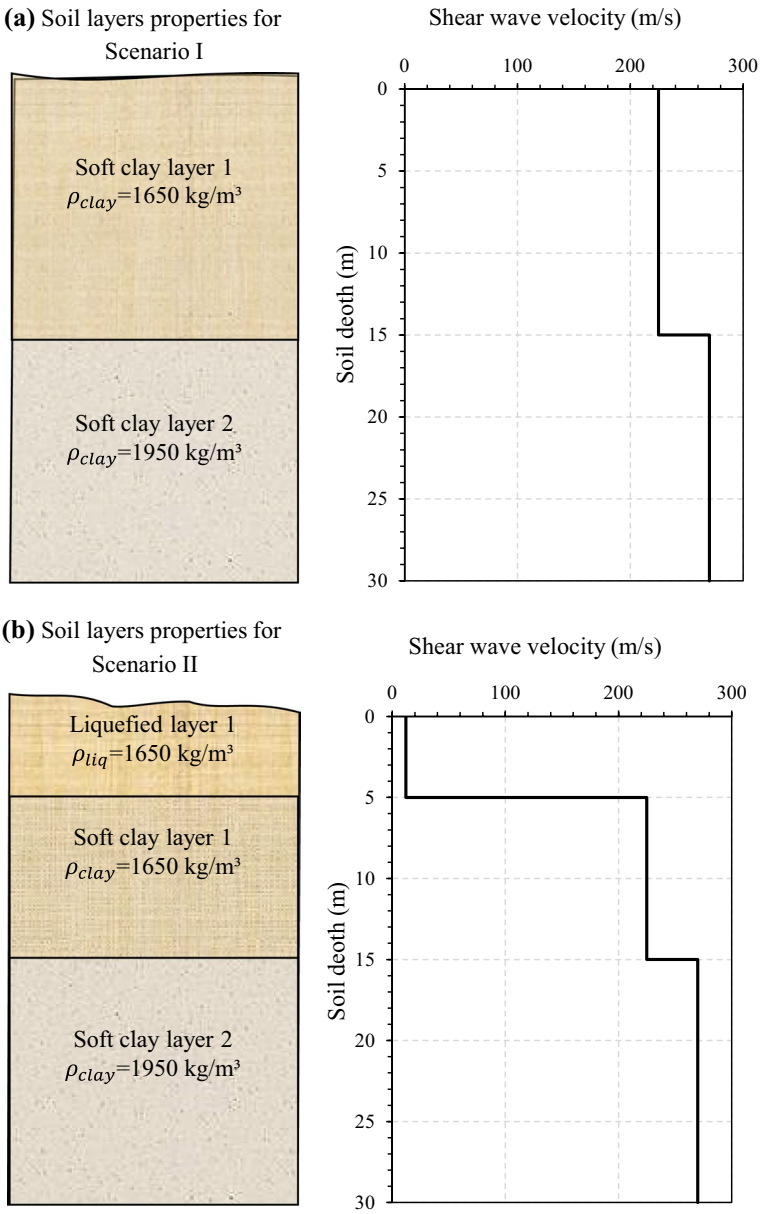

Fig. 2 Soil profile scenarios used in the study **a** Scenario I (benchmark case—non-liquefied soil); **b** Scenario II with 5.0 m deep liquefiied soil; **c** Scenario III with 10.0 m deep liquefied soil and **d** Scenario IV with 15.0 deep liquefied soil

damage of the concrete under the tensile and the compressive stresses is characterized by damage plasticity theory developed by Lubliner et al. (1989) and Lee and Dale (1998), so the adopted stress–strain relation under uniaxial tension and compression loading can be presented as follows:

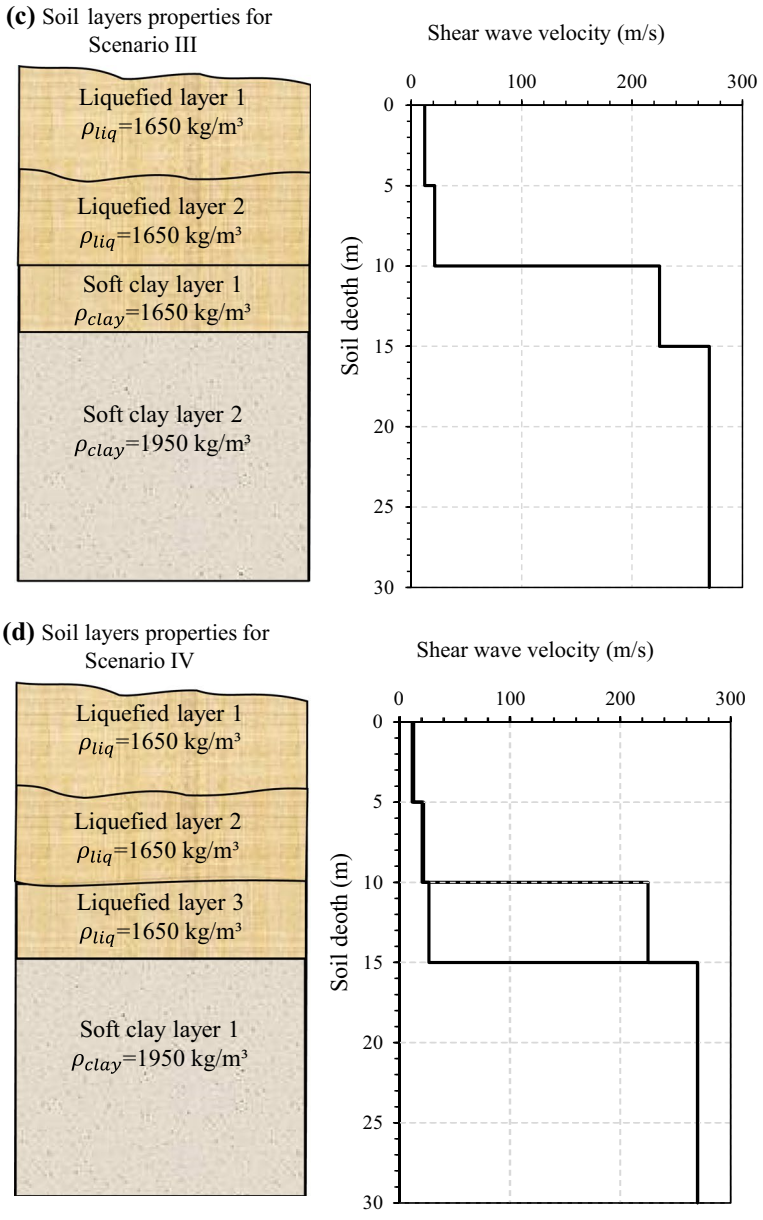

Fig. 2 (continued)

$$\sigma_t = \left(1 - d_t\right) E_0 \left(\varepsilon_t - \overline{\varepsilon}_t^{pl}\right) \tag{2}$$

$$\sigma_c = \left(1 - d_c\right) E_0 \left(\varepsilon_c - \overline{\varepsilon}_c^{pl}\right) \tag{3}$$

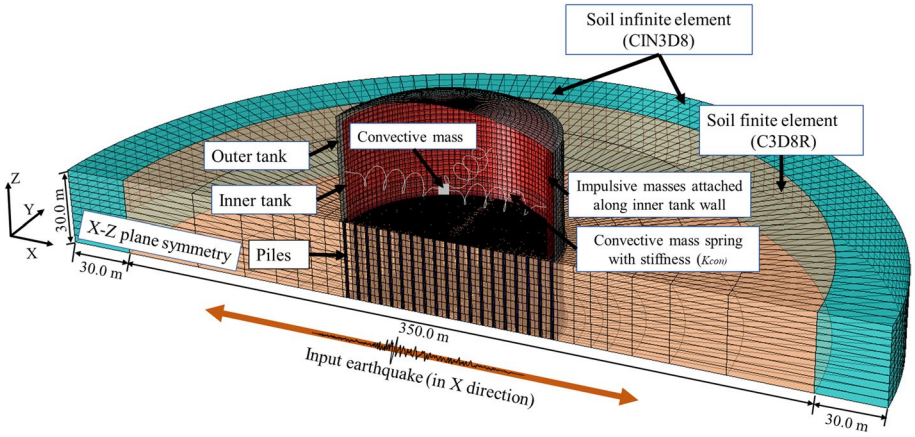

Fig. 3 The adopted finite element model used in this study for homogenous clay soil case and the modelling element details of the developed soil structure system

where the subscripts t and c refer to tension and compression, respectively, and E_0 refers to the initial stiffness of the concrete under compression and tension before any yielding occurs. The damage or degradation parameters (i.e.d_t and d_c) impacting the concrete stiffness can take a value from zero, where there is no loss in stiffness, to one, which represents the total damage state of the concrete.

Similar to many previous studies (e.g. Miglietta et al. 2016; Murray et al. 2018), the impacts that reinforcing bars would have on the concrete behaviour were modelled by introducing tension stiffening into the tension softening section of concrete damage plasticity model to simulate the load transfer across cracks through the rebar. As Wahalathantri et al. (2011) explained, by introducing tension stiffness, strain softening behaviour of the cracked concrete would be revised. The key parameter required to formulate the tension stiffening is the cracking strain $\overline{\varepsilon}_t^{cr}$, which is calculated by subtracting the elastic strain corresponding to the undamaged material from the total strain (ε_t).

$$\overline{\varepsilon}_t^{cr} = \varepsilon_t - \frac{\sigma_t}{E_0} \tag{4}$$

As discussed by Wahalathantri et al. (2011) and reported in ABAQUS (2018), the cracking strain ($\overline{\varepsilon}_t^{cr}$) and plastic strain ($\overline{\varepsilon}_t^{pl}$) are correlated as:

$$\overline{\varepsilon}_t^{pl} = \overline{\varepsilon}_t^{cr} - \frac{d_t}{\left(1 - d_t\right)} \frac{\sigma_t}{E_0} \tag{5}$$

Nayal and Rasheed (2006) reviewed different tension stiffening models, then developed a model based on the homogenized stress–strain relationship established by Gilbert and Warner (1978), which accounts for tension stiffening, softening and local bond slip effects. This model captures the response caused by primary and secondary cracking phenomena on the stress–strain graph. As this model is applicable to both steel bar reinforced and fibre reinforced concrete with only minor changes, Wahalathantri et al. (2011) modified the model to be consistent with the general formulations on CDP model available in ABAQUS. Figure 4 represents the modified tension stiffening model

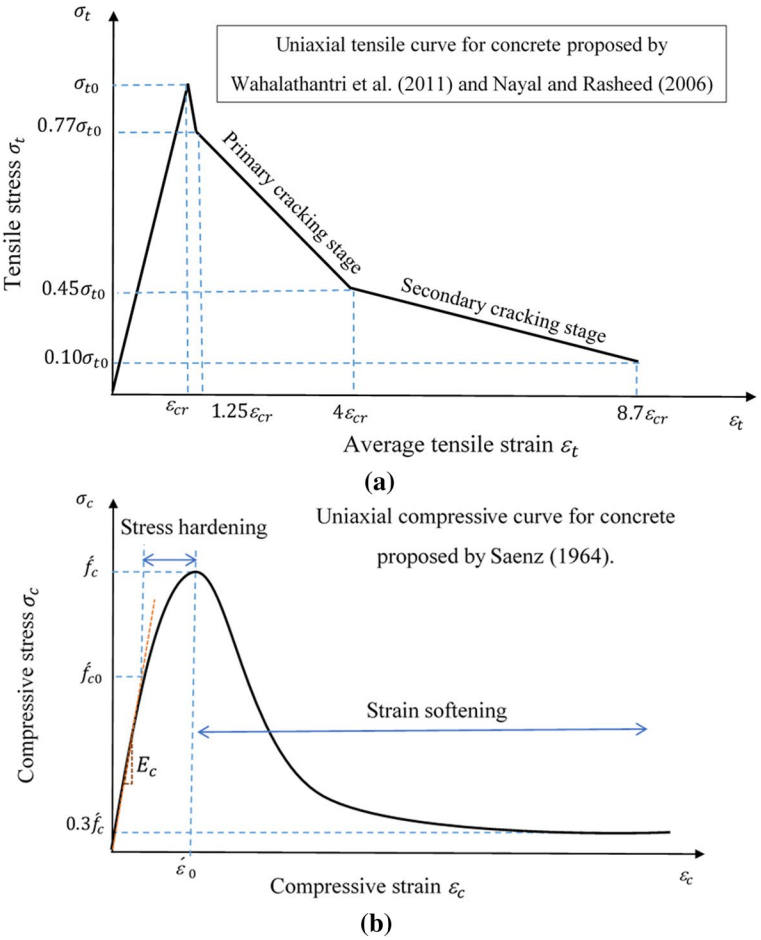

Fig. 4 Concrete damage plasticity models used in this study **a** modified tension stiffening model and **b** uniaxial compressive stress- strain curve for concrete

implemented in this study. Indeed, the stress–strain relation is linear till reaching the tensile strength σ_{t0} (MPa), where it can be determined according to ACI 318-08 (2014) as below:

$$\sigma_{t0} = 0.62\sqrt{f_c'} \tag{6}$$

where f_c' is the concrete compressive strength in (MPa). The axial strain corresponding to peak tensile strength σ_{t0} is called critical tensile strain ε_{cr}. Then there is a rather abrupt drop in the state of stress to point ($1.25\ \varepsilon_{cr}$, $0.77\sigma_{t0}$). The primary cracking stage ends at ($4\varepsilon_{cr}$, $0.45\sigma_{t0}$), while the secondary cracking stage stopes at ($8.7\varepsilon_{cr}$, $0.10\ \sigma_{t0}$) as shown in Fig. 4a.

However, to capture the compressive stress–strain behaviour of the concrete following the initial elastic response, the compressive stress data are input in terms of the inelastic crushing strain $\overline{\varepsilon}_c^{in}$ which is defined as:

$$\bar{\varepsilon}_c^{in} = \varepsilon_c - \frac{\sigma_c}{E_0} \tag{7}$$

while the plastic strains $\bar{\varepsilon}_c^{pl}$ required for evolution of the yield surface were calculated based on the recommendation by Genikomsou and Polak (2015) as follows:

$$\bar{\varepsilon}_c^{pl} = \bar{\varepsilon}_c^{in} - \frac{d_c}{\left(1 - d_c\right)} \frac{\sigma_c}{E_0} \tag{8}$$

To establish the compressive stress–strain behaviour of concrete to be used for the calibration of the CDP model parameters, data and approach provided by Saenz (1964), shown in Fig. 4b, were utilised in this study. It should be noted that many other researchers (e.g. Asran et al. 2016; Tahnat et al. 2018; and Sakr et al. 2019) had validated and utilised the compressive stress–strain relationship developed by Saenz (1964) for various grades of concrete.

For the concrete *C45* grade (i.e. $f_c' = 45$ MPa) adopted in this study for the outer reinforced concrete containment, the modulus of elasticity of concrete (MPa) was determined based on ACI 318-08 (2014) as $E_c = 0.0043 * \rho_c^{1.5} \sqrt{f_c'}$, where ρ_c is concrete density (kg/m^3) taken as 2500 kg/m^3 in this study. The basic parameters of grade *C45* concrete corresponding to the calibrated CDP model are summarised in Table 1. In addition to these parameters, variations of the compressive yield stress and the stiffness degradation with inelastic strains (i.e. $\sigma_c - \bar{\varepsilon}_c^{in}$ and $d_c - \bar{\varepsilon}_c^{in}$), as well as variations of the tensile yield stresses and the stiffness degradation with cracking strains (i.e. $\sigma_t - \bar{\varepsilon}_t^{cr}$ and $d_t - \bar{\varepsilon}_t^{cr}$), illustrated in Fig. 5, were adopted as the input parameters in this study. Indeed, Fig. 5 shows the comparison of the typical *C45* concrete response obtained from Saenz (1964) and Wahalathantri et al. (2011) for compression and tension, respectively and calibrated CDP model predictions adopting model parameters reported in Table 1. A reasonable agreement is observed, which is confirming the suitability of adopted concrete model parameters in this study.

The steel reinforcement bars in the outer concrete tank were Grade 60 ($f_y = 420$ MPa) referring to ASTM A615 (2018), and were embedded in concrete in both vertical and circumferential directions with reinforcement content ratio 1% in both directions. The rebars were modelled as an equivalent smeared layer with a constant thickness determined based on the rebar size and spacing, while adopting rebar layered shell option available in ABAQUS, particularly customised for reinforced concrete simulation as mention earlier. In this study, it is assumed that the rebar layers were completely bonded to the concrete

Table 1 Parameters used in this study to simulate the *C45* concrete adopting CDP model

Property	Symbol	Value	Reference
Density (kg/m^3)	ρ_c	2500	Ruiz and Gutiérrez (2015)
Poisson's Ratio	ν	0.2	Ruiz and Gutiérrez (2015)
Modulus of Elasticity (GPa)	E_c	36.057	ACI 318 (2014)
Dilation angle	ψ	36°	Kmiecik and Kamiński (2011)
Eccentricity	$\in$	0.1	Vermeer (1984)
Ratio of biaxial to uniaxial compressive yield strengths	f_{b0}/f_{c0}	1.16	Kupfer et al. (1969)
Ratio of the tensile to the compressive meridian	K_c	0.667	Oller (2014)

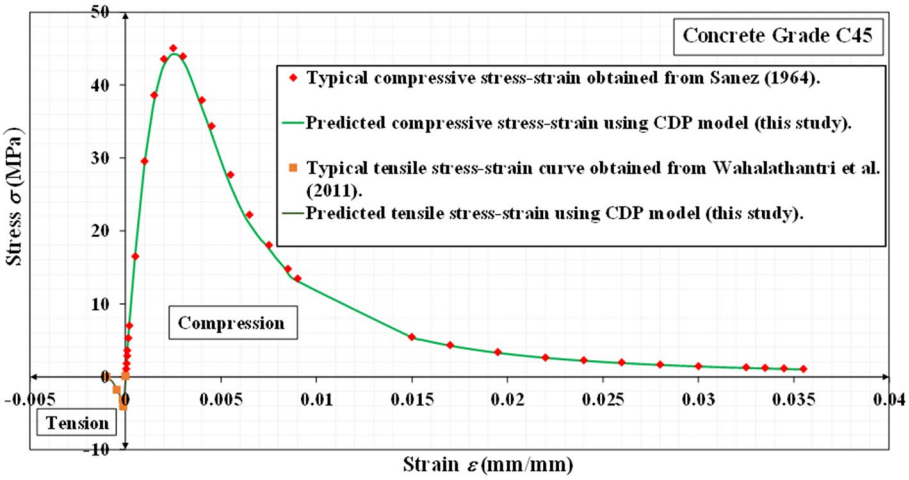

Fig. 5 Calibration of the CDP model parameters used in this study

and the linear kinematic model explained earlier was used to model the steel reinforcement bars, with adopted model parameters summarised in Table 2. It should be noted that the outer reinforced concrete tank has a fixed reinforced concrete roof, and in this study the roof material is assumed to be same as the tank wall with same reinforcement ratios.

3.1.2 Modelling of reinforced concrete piles

For the simulation of concrete piles, concrete grade *C40* ($f'_c = 40$ MPa) was adopted in this study. The hybrid modelling technique was used in this study to capture the elastic–plastic response of the piles by implementing the moment–curvature relationship for the reinforced concrete pile section, where a 2-node linear beam element (B31) was circumscribed by solid eight-node brick elements (C3D8R) with a minimal flexural rigidity (i.e. 10^6 times less than the beam elements of the pile) as used by several other researchers (e.g. Anastasopoulos et al. 2013; Rasouli and Fatahi 2021). Considering the pile geometrical characteristics and reinforcement content, the bending moment–curvature relationship of the piles was established as in Fig. 6 using SAP2000 software, and assigned to the beam element in the centre of concrete pile. It should be noted that other general beam section

Table 2 Reinforcing bar parameters adopted in this study to simulate steel Grade 60

Parameter	Symbol	Value	Reference
Tensile strength (MPa)	f_{ult}	620	ASTM A615/ A615M-18e1 (2018)
Tensile yield stress (MPa)	f_y	420	
Elongation (%)	δ	9	
Linear kinematic hardening modulus (MPa)	C_r	2222	
Young's Modulus (GPa)	E_r	206.56	Hawileh et al. (2009)
Density (kg/m^3)	ρ_r	7850	
Poisson's Ratio	v	0.3	

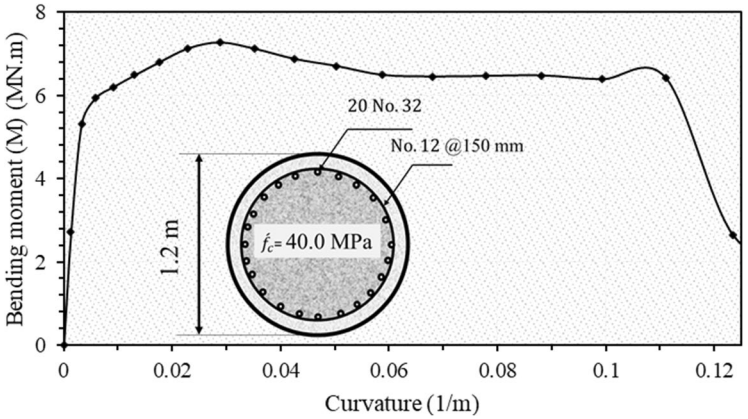

Fig. 6 Moment–curvature response of the concrete reinforced pile section adopted in this study with the pile cross section details

details including the Young's modulus of 30.1 GPa, the Poisson's ratio of 0.3, and the mass density of 2500 kg/m^3 were assigned to the pile element.

3.1.3 Modelling of inner 9% Ni steel tank

The linear kinematic hardening model was adopted in this study to model the inelastic behaviour of the inner steel tank made of 9% Ni steel, recognized by the ASTM A353 (2014) for cryogenic service temperatures, while considering linear elastic behaviour when the stress state is within the yield surface. The linear kinematic hardening model was used in several previous research studies for seismic analysis of steel structures (e.g. Zakavi and Nourbakhsh 2014; Mizuno et al. 2014). The adopted constitutive model to simulate the metal inelastic behaviour under cyclic loading, adopts Von Mises yield surface as defined in Eq. (9). In this model, the equivalent Mises stress (i.e. $f(\sigma - \alpha)$) is defined with respect to kinematic shift stress (also known as the back-stress α) which describes the translation of the yield surface in the stress space. It should be noted that in Eq. (9), the yield stress σ_y defines the size of yield surface which separates elastic and elastoplastic responses.

$$F = f(\sigma - \alpha) - \sigma_y = 0 \tag{9}$$

where σ_y is the yield stress and $f(\sigma - \alpha)$ is the equivalent Mises stress with respect to the back stress, α, which determines the kinematic evolution of the yield surface in the stress space. The adopted linear kinematic hardening model in this study assumes associated plastic flow rule which is acceptable for metals subjected to cyclic loading (Chun et al. 2002; Hashiguchi and Ueno 2017; Koo et al. 2019). The evolution of the hardening law adopted in this study follows the linear Ziegler (1959) hardening law as formulated below:

$$\dot{\alpha} = C_s \frac{1}{\sigma_y}(\sigma - \alpha)\dot{\bar{\varepsilon}}^{pl} \tag{10}$$

where $\dot{\bar{\varepsilon}}^{pl}$ is the equivalent plastic strain rate, C_s is the kinematic hardening modulus for steel which remains constant in this model, and σ_y is the equivalent stress defining the size of the yield surface which remains constant and equal to yield stress at zero plastic strain

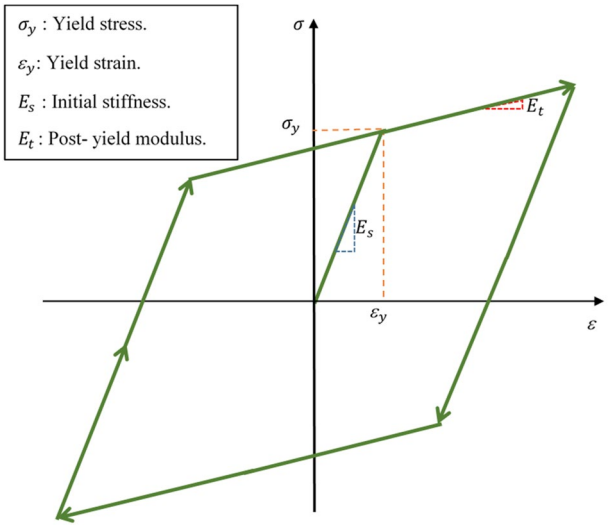

Fig. 7 Hysteresis linear kinematic hardening model adopted

$(\sigma|_0)$. In this model the kinematic hardening component is defined to be a purely kinematic following the linear Ziegler (1959) hardening law, and the relaxation term (or the recall term $\gamma_k \alpha \bar{\varepsilon}^{pl}$ mentioned in Eq. 23) is omitted since γ_k is assumed to be equal to zero.

As explained by Driver et al. (1998), the linear kinematic hardening model adopted here takes the Bauschinger effect into consideration. In other words, the model allows the straining in one direction (e.g. tension of compression) decrease the yield stress in the opposite direction (i.e. compression and tension correspondingly). Figure 7 illustrates the adopted stress–strain behaviour considering the linear kinematic hardening model with hysteresis effects to simulate response of 9% Ni steel. Indeed, the stress–strain relation follows linear elastic behaviour with initial stiffness E_s until the yield condition at point $(\sigma_y, \varepsilon_y)$ is reached. Then the stress–strain relationship continues with a post-yield modulus E_t. As shown in Figs. 7 and 8, it should be noted that the post yield modulus is different from the plastic modulus; the post yield modulus refers to the slope of the total strain and stress, while the plastic modulus (i.e. C_s) is the slop of the plastic strain versus stress. Furthermore, the inelastic material properties must be input into ABAQUS as Cauchy stress σ_{true} and true logarithmic strain ε_{true} values, which can be calculated from the nominal stress-strain values $(\sigma_{eng}, \varepsilon_{eng})$ using Lubliner (1990) equations:

$$\sigma_{true} = \sigma_{eng}\left(1 + \varepsilon_{eng}\right) \tag{11}$$

$$_{true} = ln\left(1 + \varepsilon_{eng}\right) \tag{12}$$

The inelastic input parameters for this model into ABAQUS are only two data pairs, the yield stress at zero plastic strain $\sigma|_0$, and the yield stress σ_y at finite plastic strain ε^{pl}; which are used to determine the linear kinematic hardening modulus (i.e. plastic modulus) from the following relation:

$$C_s = \frac{\sigma - \sigma|^{\circ}}{\varepsilon^{pl}} \tag{13}$$

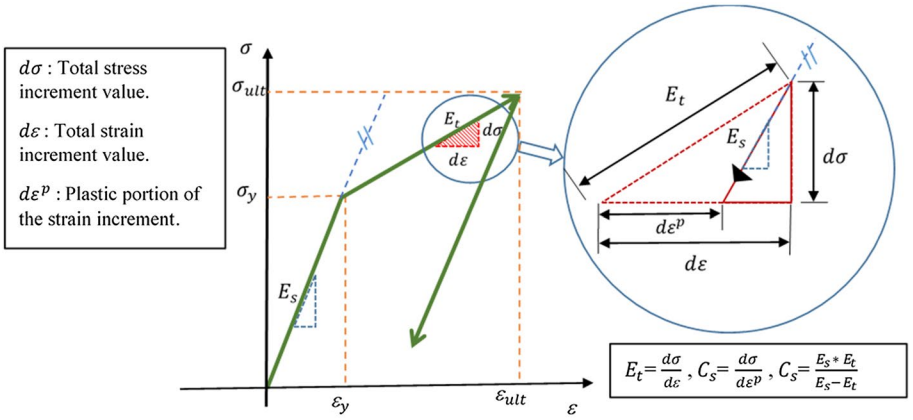

Fig. 8 The relation between the initial stiffness, tangent modulus and initial kinematic hardening modulus of the steel

The linear kinematic hardening model parameters for 9% Ni steel used in this study is summarized in Table 3.

3.2 Modelling of the fluid–structure interaction

The hydrodynamic forces exerted from the accelerated fluid to the tank walls are commonly considered in two main modes of vibration; one is due to the rigid movement of the fluid which is called the impulsive force, while the other mode is due to surface waves and sloshing of the liquid, called convective force. In practical analysis and design, these forces are represented using simplified mechanical spring-mass models (Houser 1957), where these two forces are modelled as concentrated equivalent masses attached to the tank wall via link or spring elements with appropriate stiffness. Further developments were done by Virella et al. (2006) by adopting distributed masses, also recognized by Eurocode-8 (2006), which is known as a rigorous and a sound alternative model to Houser (1957) simplified mechanical model. In Virella et al. (2006) model, instead of using one concentrated mass to represent the impulsive force, the mass is distributed along the tank wall in several segments as added masses. Indeed, usually these distributed masses are attached to the wall nodes via rigid springs. In general, the

Table 3 Linear kinematic hardening model parameters for inner 9% Ni steel tank used in this study

Property	Symbol	Value	Reference
Ultimate stress (MPa)	σ_{ult}	662	El-Batahgy et al. (2018)
Yield stress (MPa)	σ_y	515	
Elongation (%)	δ	28	
Linear kinematic hardening modulus (MPa)	C_s	275	
Young's Modulus (GPa)	E_s	205	Aggen and Allen (2018)
Density (kg/m^3)	ρ_{steel}	7850	
Poisson's Ratio	ν	0.29	

Virella et al. (2006) replaced the hydrodynamic concentrated forces of Houser (1957) mechanical model with equivalent distributed pressure along the tank wall.

In this study, the FSI was considered by combining the Houser (1957) spring-mass model and the distributed pressure method of Virella et al. (2006). Indeed, the concentrated convective mass was used to model the convective force based on Houser (1957) and API-650 (2007), while the impulsive mass model based on Virella et al. (2006) and Eurocode-8 (2006) pressure distribution method was used to simulate the impulsive force. The adopted techniques deem suitable since the convective mode is generally uncoupled and independent from the impulsive mode, and can have less impact on the overall response of the liquid storage tank under horizontal loading, and many previous studies ignored the convective mode of liquid when adopting the add-mass approach for the sake of simplicity (e.g. Virella et al. 2006; Buratti and Tavano 2014).

As mentioned above, the convective force was modelled using spring—mass model, including the first convective mode of vibration only for the single convective mass (i.e. M_{con}) attached to the inner tank at a height of H_{con} (the centre of action or effective height of the convective mass) via springs with a stiffness equal to $K_{con,}$ where in this study the springs were used to connect the convective mass to the tank wall in the horizontal direction (i.e. earthquake acceleration direction). The required parameters to capture the convective hydrodynamic effect were determined using the following equations (API-650 2007):

$$M_{con} = 0.23\frac{D}{H}\tanh\left(3.67 * \frac{H}{D}\right) * M_{total} \tag{14}$$

$$C_{con} = \frac{0.578}{\sqrt{\tanh\left(3.68 * \frac{H}{D}\right)}} \tag{15}$$

$$K_{con} = \left(2 * \pi * \frac{M_{con}}{T_{con}}\right)^2 \tag{16}$$

$$H_{con} = \frac{\cosh\left(3.68 * \frac{H}{D}\right) - 1}{\tanh\left(3.68 * \frac{H}{D}\right) sinh\left(3.68 * \frac{H}{D}\right)} \tag{17}$$

where M_{con} is convective mass, M_{total} is the total mass of liquid in the tank, T_{con} is the convective period, C_{con} is sloshing period coefficient, K_{con} is the effective stiffness for the convective mode (N/m), H_{con} is the convective mass height, and H and D are the liquid height and tank radius, respectively.

For the impulsive mass modelling, Eurocode-8 (2006) was used, in which the spatial–temporal distribution of the rigid impulsive component of the hydrodynamic pressure (p_{imp}) were determined by the following expressions to obtain the distributed impulsive masses m_{imp}:

$$p_{imp}(\xi, \varsigma, \theta, t) = C_{imp}(\xi, \varsigma)\rho R_{tank} \times A_g(t) \tag{18}$$

$$C_{imp}(\xi,\varsigma)=2\gamma\sum_{n=0}^{\infty}\frac{(-1^{n})}{\left(I_{1}'\left(\frac{\nu_{n}}{\gamma l}\right)\right)\nu_{n}^{2}}\cos\left(\nu_{n}\varsigma\right)I_{1}\left(\frac{\nu_{n}}{\gamma l}\xi\right) \tag{19}$$

$$m_{imp}=\frac{p_{imp}\Delta h}{A_{g}(t)} \tag{20}$$

where $\xi=r/R_{\text{tank}}$ and $\varsigma=z/H_{L}$ are the non-dimensional coordinates, R_{tank} is the radius of the tank, r, θ, z are components of cylindrical coordinates with origin at the centre of the tank while the z axis is vertical, t is time, C_{imp} is impulsive pressure distribution coefficient, $\nu_{n}=((2n+1)/1)\,\pi$, $\gamma 1=H_{L}/R$, I_{1}, I_{1} are the modified Bessel functions of order 1 and its derivatives, respectively, $A_{g}(t)$ is the horizontal ground acceleration time history in the free-field condition, and ρ is the mass density of the fluid. Indeed, Eq. (20) was used to calculate the equivalent mass at each segment of tank wall, which was 1.0 m segment along the tank wall in this study. As recommended by Virella et al. (2006), a convenient alternative to avoid attaching lumped masses via rigid link elements, is including these extra masses by increasing the wall density in each segment, which was used in this study to reduce the computational time.

3.3 Modelling of the soil deposit

3.3.1 Modelling of clay soil deposit

The nonlinear kinematic hardening model, was implemented in this study to model the cyclic behaviour of clay (non-liquefiable soil) under seismic loading. This pressure-independent plasticity model based on Von Mises yield criteria, and associated flow rule, can be considered as appropriate model for nonlinear cyclic behaviour of pressure independent material, such as clay under undrained condition (Zhang and Tang 2007). As explained by George et al. (2016) and Zhu (2019), the key parameters of this model are Young's modulus, Poisson's ratio, and stress–strain curve of stabilised loading cycle obtained from the triaxial shear test. Based on the modification work done by Armstrong and Frederick (1966) on the original model which was proposed by Lemaitre and Chaboche (1994), the yield surface of the adopted nonlinear kinematic hardening constitutive model is defined according to Eq. (9), while the equivalent Mises stress can be defined by the following relation:

$$f(\sigma-\alpha)=\sqrt{\frac{3}{2}\left(S-\alpha^{dev}\right):\left(S-\alpha^{dev}\right)} \tag{21}$$

where S is the deviatoric stress tensor, and α^{dev} is the deviatoric part of back stress tensor. In the adopted model, an associated flow rule is adopted to obtain the required kinematic hardening flow rule as reported by Zhu (2019). The hardening rule of this model is a mixed nonlinear isotropic-kinematic hardening making it suitable for simulating cyclic behaviour of soils as explained by Elia and Rouainia (2016) and Mucciacciaro and Sica (2018). Indeed, the nonlinear kinematic hardening component describes the translation of the yield surface in stress space through the back stress (α), as it is defined by the superposition of pure kinematic and relaxation (source of the nonlinear behaviour) terms, while the isotropic hardening component describes the change of the equivalent stress defining the

size of the yield surface (σ_y) as a function of plastic deformation. The isotropic hardening behaviour adopted in this study follows a simple exponential law as reported by ABAQUS (2018) and Zhu (2019) and presented in Eq. (22), and data fitting can be utilised to obtain the model parameters by directly introducing data points for the yield surface size and plastic strains.

$$\sigma_y = \sigma|_0 + Q\infty\left(1 - e^{-b\overline{\varepsilon}^{pl}}\right) \tag{22}$$

where $\sigma|_0$ is the yield stress at zero plastic strain and $Q\infty$ and b are material parameters, corresponding to the maximum change in the size of the yield surface, and the parameter defining the rate at which the size of the yield surface changes as plastic straining develops, respectively. It should be noted that when the equivalent stress defining the size of the yield surface remains unchanged (*i.e.*$\sigma_y = \sigma|_0$), the general combined nonlinear isotropic-kinematic hardening model reduces to a nonlinear kinematic hardening model, which is adopted in this study.

The evolution of the kinematic component for the yield surface on the stress space based on Ziegler (1959) kinematic hardening law is presented below:

$$\dot{\alpha}_k = C_k \frac{1}{\sigma_y}(\sigma - \alpha)\dot{\overline{\varepsilon}}^{pl} - \gamma_k \alpha \dot{\overline{\varepsilon}}^{pl} \tag{23}$$

where (α_k) is the back-stress tensor, C_k and γ_k are material parameters for each back stressα_k, which are obtained through calibration using cyclic test data. Indeed, C_k is the initial kinematic hardening moduli, and γ_k determines the rate at which the kinematic hardening moduli decreases with the plastic strains for each back stress α_k. It should be noted that the recall term $\gamma_k \alpha \dot{\overline{\varepsilon}}^{pl}$ introduces the nonlinearity to the evolution law proposed by Chaboche and Lemaitre (1990).

Moreover, each back stress is covering a different range of equivalent plastic strains, so the overall back stress is computed by summation of back stresses:

$$\alpha = \sum_{k=1}^{N} \alpha_k \tag{24}$$

The kinematic and isotropic hardening components are illustrated in Fig. 9a for uniaxial loading, while Fig. 9b illustrates the same for more generalised stresses for multiaxial loading. It is evident that the kinematic hardening component implies that the back stress is contained within a cylinder of radius $\sqrt{\frac{2}{3}}\alpha^s$, where α^s is the magnitude of α at large plastic strains (known as saturation condition), while the stress points lie within a cylinder with radius $\sqrt{\frac{2}{3}}\sigma_{max}$ (represented in Fig. 9) since the yield surface remains bounded.

As explained above, the adopted nonlinear kinematic hardening model requires input parameters C_k and γ_k, or directly input triaxial shear test data corresponding to the stress–strain data points for stabilised cyclic curve. In this study, the soil properties, corresponding to the site class *C* and the density and shear wave velocity taken from in-situ tests are $\rho_{\text{clay}} = 1650$ kg/m^3 and 1950 kg/m^3, with $V_s = 225$ m/s and 270 m/s, for the top 15 m and the second 15.0 m, respectively. The maximum shear modulus (G_{max}) of the adopted soil was obtained from the following relationship:

$$G_{max} = \rho_{soil} * V_s^2 \tag{25}$$

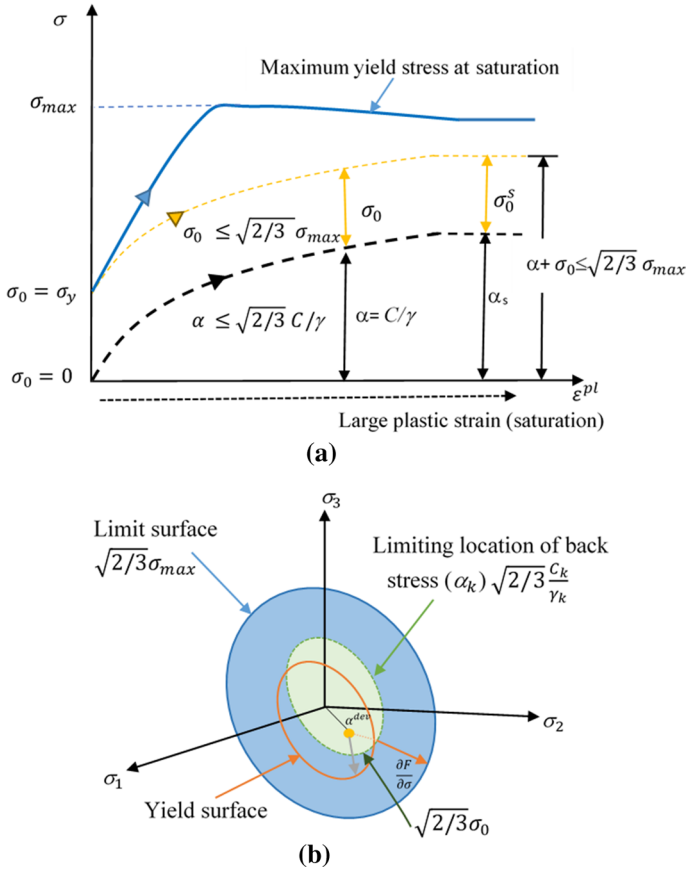

Fig. 9 Soil nonlinear kinematic model **a** One-dimensional representation of the hardening in the nonlinear isotropic/kinematic model; **b** the generalised stresses for multiaxial loading in three-dimensional representation of the hardening in the nonlinear Isotropic/kinematic model

Sun et al. (1988) recommended backbone curves for practical use in seismic site response evaluations for cohesive soils as reported in Fig. 10. The backbone curves adopted in this study capture the variations of modulus reduction ratio (G/G_{max}) and damping ratio (ξ) with cyclic shear strain (γ) for cohesive soils obtained from cyclic simple shear and resonant column test results. To obtained an analytical formulation fitting the backbone laboratory measurements, Hardin and Drnevich (1972) model, as shown below, was adopted in this study.

$$\tau = \frac{G_{max}}{1 + \frac{\gamma}{\gamma_{ref}}} \tag{26}$$

$$\xi_{damping} = \xi_{max}\left(1 - \frac{G}{G_{max}}\right) \tag{27}$$

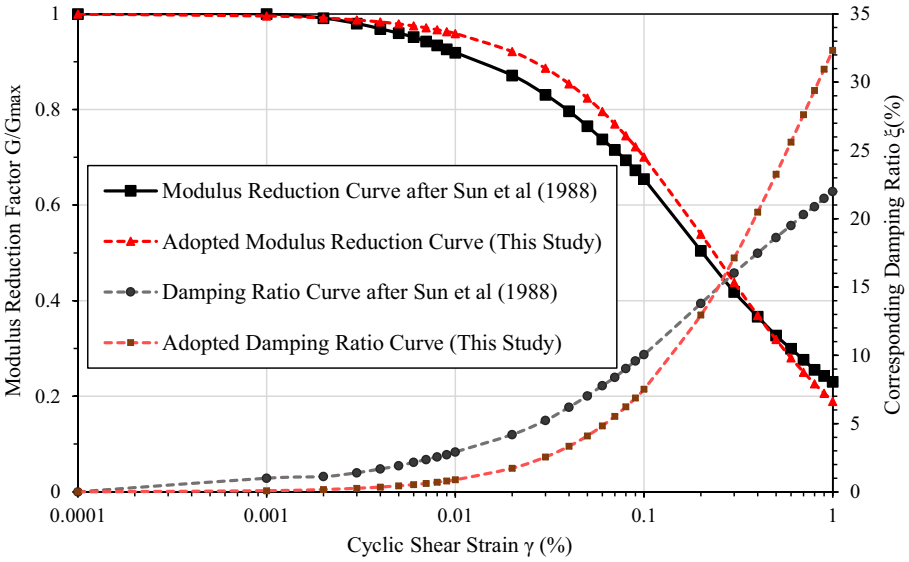

Fig. 10 Adopted fitting curve for cohesive soil in this study

where τ is the shear stress, ξ is the damping ratio, G is secant shear modulus, γ is the cyclic shear strain of the soil, and γ_{ref} is Hardin and Drnevich (1972) constant to get a best fit for backbone curves for modulus reduction and damping ratio. The calibrated value of $\gamma_{\text{ref}}=0.234$ resulted in the best match for backbone curves with coefficient of determination R^2 equal to 0.88 and 0.80 for the modulus reduction curve and damping ratio, respectively, as evident in Fig. 10.

Since the kinematic hardening model adopted in this study for cyclic behaviours of soils required the stabilised stress–strain cycle, Masing (1926) rule presented in Eq. (28) was used to obtain the cyclic shear stress–strain behaviour. In this study, it is assumed that the stabilised cyclic loading–unloading curve is reached at cyclic shear strain value of 2% beyond which the shear modulus remains unchanged.

$$\tau - \tau_{rev} = \frac{G_{max}(\gamma - \gamma_{rev})}{1 + \left(\frac{|\gamma - \gamma_{rev}|}{2 * \gamma_{ref}}\right)} \tag{28}$$

where τ_{rev} and γ_{rev} are the shear stress and cyclic shear strain at the reversal point.

The stabilised loading cyclic was used to obtain the kinematic hardening parameters by inputting the shear stress and plastic shear strain data points from the re-yielding point to the reversal point. Indeed, using an ABAQUS subroutine, a curve fit analysis was conducted to determine the combined hardening constants based on the shear–stress strain data points. Referring to Eq. (24), by adopting several back stresses and calibrating the parameters, a larger strain range can be covered resulting in more accurate predictions. Thus, in this study two back stresses were adopted which resulted in more reliable predictions. Table 4 summarises soil properties and the calibrated kinematic hardening model parameters adopted in this study.

Table 4 Clay soil properties and calibrated nonlinear kinematic hardening model parameters

Soil properties	Symbol	Value for Soft clay layer 1	Value for Soft clay layer 2
Density (kg/m^3)	ρ_{clay}	1750	1950
Undrained shear strength (kPa)	Cu	18.5	24
Shear wave velocity (m/s)	V_s	225	270
Small strain shear modulus (MPa)	G_{max}	88.1	142.1
Poisson's Ratio	ν	0.3	0.49
Calibrated initial kinematic hardening modulus (MPa)	C_{k1}, C_{k2}	26.1, 250	45.9, 280
Calibrated hardening modulus decreasing rate	γ_{k1} and γ_{k2}	1150, 1450	1170.36, 1600

Figure 11 illustrates the comparison of the calibrated kinematic hardening model adopted in this study versus the laboratory measurements obtained from Sun et al. (1988) experiments while adopting Masing (1926) rule to obtain closed loading–unloading cyclic loop. As evident, the predictions adopting kinematic hardening model are in good agreement with the experimental data, confirming the suitability of the adopted nonlinear kinematic hardening model and calibrated parameters to simulate the cyclic response of adopted soft clay deposits.

3.3.2 Modelling of liquefied soil deposit

During an earthquake, the rapid shaking of the ground can generate large pore water pressures in saturated loose granular soils under undrained condition which results in a reduction in effective stresses and subsequently a substantial loss in strength and stiffness. The variables that influence the onset of liquefaction mainly include the presence of groundwater, the particle size distribution of the soil, the in-situ relative density of the soil, the effective confining stress and the amplitude and duration of ground motions.

The current state-of-the-practice approach commonly adopted in projects has been used to obtain the post-liquefaction properties of the liquifiable layers for modelling. The adopted approach is in accordance with Idriss and Boulanger (2008), where the residual shear resistance of liquefied sand, *Sr*, were estimated based on back analysis of several field case histories. Idriss and Boulanger (2008) correlated the residual shear strength with the ground in-situ penetration test measurements (SPT or CPT). In this study, the correlation (Eq. 29) based on equivalent clean sand corrected SPT value, $(N1)60cs-Sr$, is adopted for condition in which the effects of void redistribution is considered negligible:

$$S_r/\sigma'_{vc} = \left(\frac{(N_1)_{60cs-Sr}}{16} + \left(\frac{(N_1)_{60cs-Sr} - 16}{21.2} \right)^3 - 3.0 \right) \leq \tan\varphi' \tag{29}$$

where S_r/σ'_{vc} is residual shear strength ratio, σ''_{vc} is effective vertical stress pre-liquefaction, and φ' is effective friction angle of the liquefiable layer (before onset of liquefaction). The idea of correlating residual strength with $(N1)60cs-Sr$ was initially proposed by Seed (1987) and considered logical on the basis of critical-state concepts and established

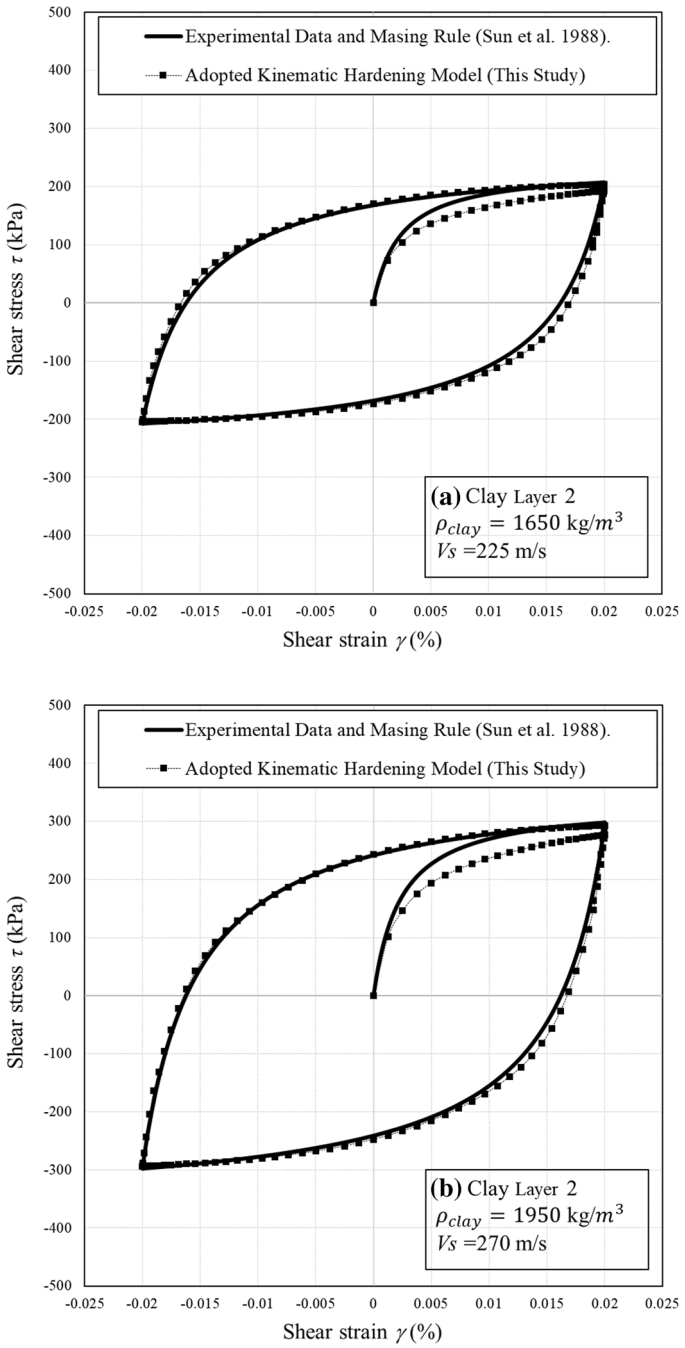

Fig. 11 Comparison of cyclic stress–strain predictions adopting the calibrated kinematic hardening model and corresponding experimental data for clayey soils **a** clay soil layer 1 (from 0.0 to 15.0 m depth) and **b** clay soil layer 2 (from 15.0 to 30.0 m depth)

correlations between the overburden correlated penetration resistance and in-situ relative density (Idriss and Boulanger 2008).

Table 5 summarizes the post-liquefaction soil properties used in this study. The damping behaviour of the liquefied soil was captured using Rayleigh damping formulation via Rayleigh damping coefficients $\alpha_{damping}$ and $\beta_{damping}$, calculated based on the first and second mode natural frequency of the liquefied soil deposit and 20% damping ratio for the liquefied soil referring to Poulos (2017), Boulanger et al. (2014) and Lombardi and Bhattacharya (2014). Rayleigh damping coefficients adopted in this study for different liquefied soil thicknesses are presented in Table 5.

3.4 Modelling of interfaces, boundary conditions and the adopted earthquakes

To include the SSI effect and capturing the possible separation or sliding between the subsoil and the piles, and between the subsoil and the foundation raft (i.e. outer tank slab), interfaces were defined between the mentioned surfaces. For the normal response of interacting surfaces, the hard contact algorithm was used by defining the relationship between the contact pressure (p) and the overclosure (h) between the master and slave surfaces. Indeed, the pressure was transferred between interacting surfaces when the overclosure between them was zero (i.e. $h=0$). In this adopted hard contact model, penalty algorithm, based on stiff approximation of contacting surfaces, was implemented to avoid over-constraining issue in the modelling, and thus a small degree of penetration for the interacting surfaces, was allowed. Moreover, for the tangential interaction between the interacting surfaces, the Coulomb frictional model via penalty formulation was implemented, where the relative movement between the contacting surfaces was controlled by defining a critical shear stress between them ($\tau_{critical} = \mu . P$), which is proportional to the contact pressure through the friction coefficient (μ), where the relative movement can occur when the shear stress between the contacting surfaces exceeds the critical shear stress (i.e. the frictional

Table 5 Post-liquefaction residual properties for sand

Soil properties	Symbol	Liquified soil layer 1	Liquified soil layer 2	Liquified soil layer 3
		Value	Value	Value
Density (kg/m^3)	ρ_{liq}		1650	
Friction angle (Degree)	Φ		0	
Poisson's Ratio	ν		0.49	
Equivalent *SPT* value	$(N_1)_{60cs-Sr}$		14	
Residual Shear Stress Ratio (based on Idriss and Boulanger, 2008)	Sr/σ'_{vo}		0.12	
Effective Stress at mid. of liquefiable layer (kPa)	σ'v	40	121	202
Residual Shear Strength (kPa)	S_r	4.85	14.5	24.3
Residual Shear Stiffness (kPa)	G_{liq}	243	728	1213
Residual Shear Wave Velocity (m/s)	$V_{s(liq.)}$	12	21	27
Adopted Rayleigh damping parameters	α	0.659	1.21	1.72
	β	0.062	0.033	0.0218

resistance between the surfaces). The friction coefficients (μ) between the clay subsoil and the raft surfaces, and between the subsoil and pile surfaces were considered to be 0.4 and 0.35, respectively (Rasouli and Fatahi 2021; Agalianos et al. 2020). It should be noted that frictionless interfaces were used between the liquefied soil and foundation elements. Moreover, the rigid connection between the pile head and the raft foundation was imposed via the tie constraint condition available in ABAQUS.

The numerical analyses for the tanks—foundation—soil system was performed in two steps; the initial step, which was static analysis, considered the gravity loads for the entire system, followed by the second step which was application of earthquake acceleration at the model base in *X*-direction only adopting dynamic implicit stepping technique. During the static analysis, the bottom of the soil deposit was fixed in all directions, and the vertical movements were allowed on the side boundaries, while the displacements normal to the side boundaries were disallowed. During the dynamic analysis, the infinite boundaries were introduced on the side boundaries replacing the initial roller boundaries. The adopted one way 8 nodes infinite elements CIN3D8 (see Fig. 3) are appropriate solid elements representing the far-field soil, capturing the initial static equilibrium conditions (Zienkiewicz et al. 1983) and absorbing the energy from the unbounded soil area under dynamic loading (Lysmer and Kuhlemeyer 1969). During the dynamic analysis the response of these elements are isotropic linear elastic and represent the infinite model where the normal waves are not allowed to be reflected and the damping of the normal velocity of these boundaries are governing by the following equations:

$$\rho c_p = \rho \sqrt{\frac{\lambda + 2G}{\rho}} \tag{30}$$

$$\rho c_{sv} = \rho \sqrt{\frac{G}{\rho}} \tag{31}$$

where c_p and c_{sv} are the compressive and shear wave velocities of the soil, ρ is the mass density of the material, and λ and G are Lamé's constants. It should be noted that the adopted infinite elements eliminate energy transmission for plane waves crossing the boundary, while the wave propagation upward will not be distorted.

For the input seismic excitations, one near-field earthquake 1999 Chi-Chi earthquake and one far-field earthquake, 1968 Hachinohe earthquake, were used to study the dynamic response of the LNG tank. In general, the seismic design of LNG tanks follows the same scenario of nuclear power plants by applying the two earthquake levels, namely the Operating Basis Earthquake (OBE) and Safe Shutdown Earthquake (SSE). Under OBE, the LNG storage system needs to remain fully operational with no damage, while subjected to SSE, no leakage of LNG should occur. In this study, the response of LNG tank system subject to SSE was assessed.

To minimise the scatter in the response of earthquake engineering demand parameters, the seismic input motions are suggested to be scaled using spectral matching method (Guzel 2019). The spectral matching which adjusts the frequency content of an accelerogram till its response spectrum almost matches a target response spectrum with the minimal alteration of the velocity and displacement histories of the record was conducted using SeismoMatch software (SEISMOSOFT 2016).

To simulate earthquake wave transmitted from bedrock (i.e. high shear wave velocity) via assessed ground condition to the LNG tank, the response spectra of input motions

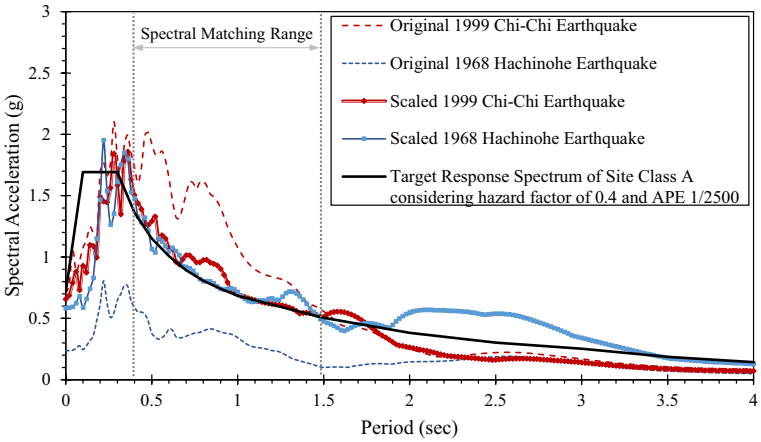

Fig. 12 The target acceleration response spectra and the original with the scaled acceleration response spectrum for the applied earthquake

were scaled to the target response spectrum representing Site Class A (i.e. strong rock site) from AS/NZS1170.5 (2004) as shown in Fig. 12. The shape of target spectrum is defined by the response spectrum acceleration factor *C(T)* using Eq. (32).

$$C(T) = C_h(T)ZR\left\{1 + (N_{max} - 1)\left[\frac{20 - D_k}{18}\right]\right\} \tag{32}$$

where $C_h(T)$ is spectral shape factor which depends on the site subsoil class and structure period (T), Z is the hazard factor equal to 0.4 for Wellington city in New Zealand based on the available site hazard map. R is the return period factor taken as 1.8 (i.e. annual probability of exceedance (APE) of 1/2500) for the SSE earthquake level for tank containing hazardous liquid based on importance level of 4 and design working life of 100 years taken from AS/NZS1170.5 (2004). N_{max} and D_k are factors related to near fault properties, where N_{max} is the maximum near fault factor and taken to be 1 in this study; and D_k is the shortest distance between the site and the nearest fault which was considered to be 2 in this study.

A specified period range, the minimum and maximum periods of 0.4 s and 1.5 s, respectively which covers the period range of soil-structure system under seismic load, was defined to perform spectral matching. Figure 13 shows the original (PEER 2014) and scaled accelerogram. It should be noted that baseline correction was conducted after the selected accelerogram being spectral matched. The scaled accelerogram was applied at the base of the soil-structure model to perform dynamic analysis.

4 Results and discussions

In this section, the results of free vibration and time history analyses are presented to assess the dynamic response of LNG tank system while capturing effect of soil liquefaction on the seismic response of the pile foundation and the superstructure. Initially, the free vibration analysis results are presented, and then numerical predictions from the nonlinear time

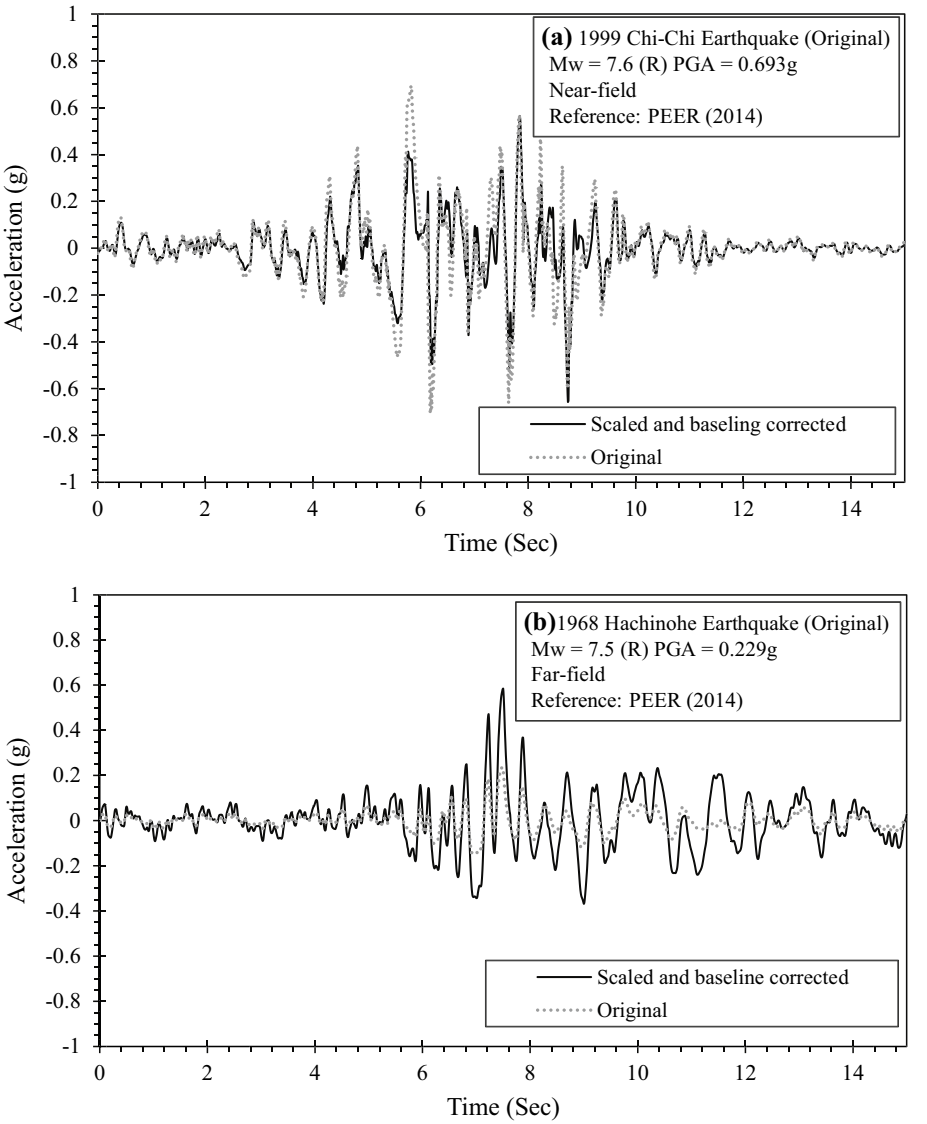

Fig. 13 Scaled earthquake records from: **a** 1999 Chi-Chi earthquake; **b** 1968 Hachinohe earthquake

history analysis under the 1999 Chi-Chi and the 1968 Hachinohe earthquakes are presented and discussed.

4.1 Free vibration analysis

In this study, the modal analysis was performed for the LNG tank using Block Lanczos algorithm. Firstly, the modal analysis on the fixed base tank (no foundation movement) was conducted as a reference to highlight importance of SSI when compared with other cases

capturing the soil and foundation movements. Since the impulsive and convective hydrodynamic forces were modelled using added mass and spring-mass methods, respectively, the first impulsive and convective modes of the LNG were captured in the numerical model and the corresponding predicted natural periods were compared with the analytical formulations available in API-650 (2007) as below:

$$T_{con} = 1.8 * C_{con} * \sqrt{D} \tag{33}$$

$$T_{imp} = C_l \frac{H_L}{\sqrt{2000 \frac{t_u}{D}}} \sqrt{\frac{\rho}{Es}} \tag{34}$$

where C_{con} is sloshing period coefficient (explained earlier in Eq. (23)), C_l is the coefficient for determining the impulsive period of tank system, which depends on the *H/D* ratio, and could be obtained from API-650 (2007), t_u is the equivalent uniform thickness of the tank wall in mm, H_L H_L H_L is the fluid design level in meter, D is the diameter of the tank in meter, Es is the modulus of elasticity of the inner tank in MPa, and ρ is the fluid density in kg/m^3, which was assumed to be 480 kg/m^3 for LNG.

Table 6 summarise the FEA predictions and the analytical calculations for the natural period of inner LNG tank. Moreover, Fig. 14a and b show the vibration mode shapes for both impulsive and convective first modes. It can be noticed that the first impulsive mode shape is the beam type mode, where the liquid and the tank wall vibrated similar to a cantilever beam as a result of rigid movement of the impulsive LNG mass attached to the tank wall. In addition, the convective mass vibrated in the horizontal direction since it was tied to the tank wall via springs controlling the stiffness of the vibrating mass. Figure 14c represents the first mode shape for outer concrete tank, and it is evident that the first mode shape corresponded to tank roof. Moreover, Table 6 verifies the suitability of the proposed mechanical model to simulate fluid–structure interaction (FSI) in the three-dimensional finite element model used in this study, since a good agreement was observed between the natural periods obtained from the 3D numerical and the analytical formulations in API-650 (2007).

The effects of the soil liquefaction on the dynamic properties of LNG tank supported by end-bearing pile foundation namely frequency and damping are also discussed. Table 7 summarise the results of the modal analysis conducted to obtain the natural frequency of the LNG tank for different depths of liquefied soil deposit varying from zero (no liquefaction) to 15 m. In general, the vibration characteristics of pile foundation impact the response of the entire LNG tank system. Indeed, Table 7 show that the natural period of the LNG tank system increased significantly when the soil deposit liquefied; for example, the fundamental period of the LNG tank excluding soil liquefaction was 0.46 s, while when

Table 6 The fundamental periods of vibration obtained from numerical model and analytical solution

Method of calculation	FEM Calculation (this study)	API-650 (2007) Approximation
Impulsive fundamental period T_{imp} (sec)	0.334	0.354
Convective fundamental period T_{con} (sec)	10.42	9.67
Outer tank fundamental period T_{outer} (sec)	0.146	–

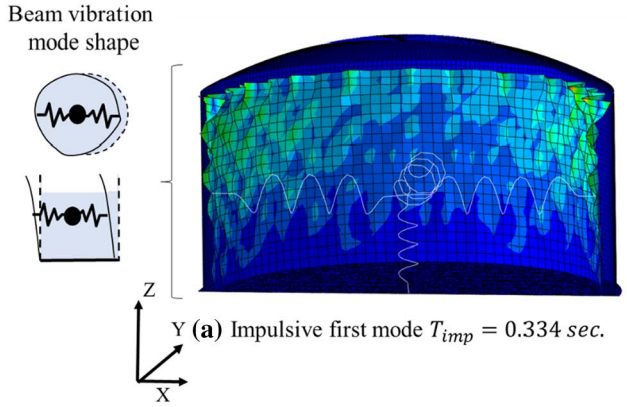

(a) Impulsive first mode $T_{imp} = 0.334\ sec.$

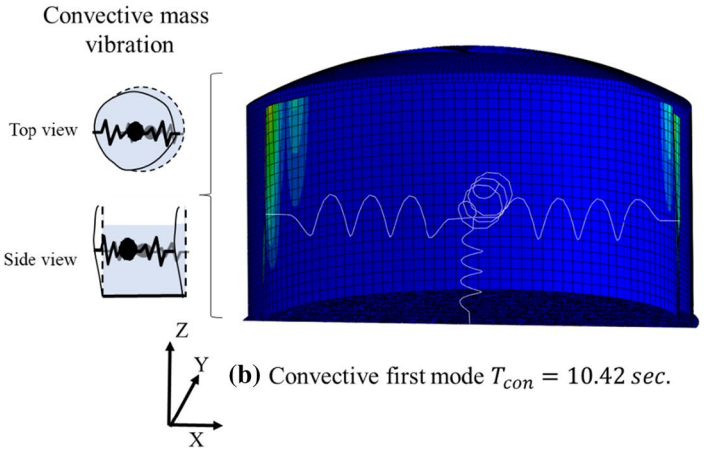

(b) Convective first mode $T_{con} = 10.42\ sec.$

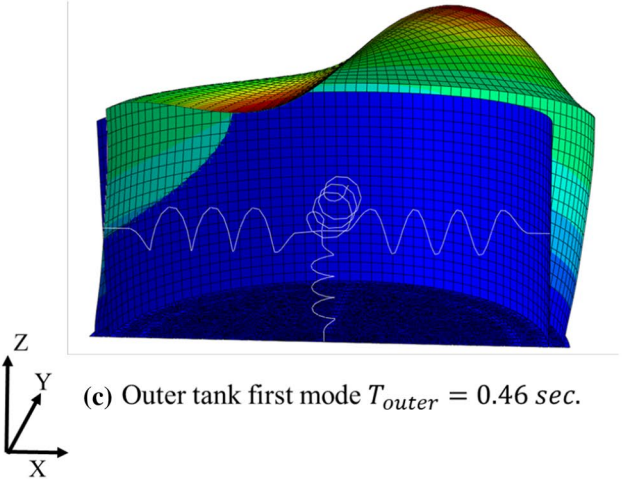

(c) Outer tank first mode $T_{outer} = 0.46\ sec.$

Fig. 14 Fixed based LNG tank free vibration mode shapes for the Inner and outer tanks; **a** Impulsive **b** convective modes for the proposed mechanical model used in this study, and **c** the outer tank first mode shape

Table 7 Variations of natural frequencies of LNG tank with different sub soil conditions

Sub soil condition	LNG tank natural period							
	Convective mode period (sec)		Impulsive mode period (sec)		Outer tank mode period (sec)		Pile foundation system period (sec)	
	First mode (T_1)	Second mode (T_2)	First mode (T_1)	Second mode (T_2)	First mode (T_1)	Second mode (T_2)	First mode (T_1)	Second mode (T_2)
Fixed base condition	10.24	5.33	0.334*	0.21	0.146	0.128	–	–
Scenario I (Non-liquefied, T_{s1})	10.238	5.32	0.51	0.395	0.248	0.24	0.46*	0.32
Scenario II (5 m deep liquefied soil, T_{s2})	10.16	5.2	0.78	0.67	0.56	0.53	0.78*	0.67
Scenario III (10.0 m deep liquefied soil, T_{s3})	9.78	4.82	0.94	0.91	0.627	0.613	0.94*	0.89
Scenario IV (15.0 m deep liquefied soil, T_{s4})	9.5	4.23	1.17	1.08	0.74	0.72	1.17*	1.0

*The fundamental natural period (sec)

the top 5 m of soil liquefied, the fundamental natural period increased by 69% to 0.78 s. This is due to the fact that loss of soil stiffness around the piles supporting the LNG tank as a result of liquefaction increased the overall structural flexibility and thus altered the dynamic characteristics of the LNG tank system significantly. Further increasing the depth of liquefied soil to 10 m and 15 m, increased the natural period of the LNG tank system by 104% (to 0.94 s) and 154% (to 1.17 s) comparing to the LNG tank on non-liquefiable soil, respectively. Figure 15 shows the corresponding fundamental vibration mode shapes for LNG tank. When the soil deposit liquefied, the mode shape was governed by the vibration of the section of the pile embedded in the liquefied soil layer which deform more compared with the pile in the non-liquefied soil deposit. In general, when the soil liquefied and the liquefaction extended deeper, the dynamic properties of the LNG tank alerted significantly, which could trigger different responses for different parts of the LNG tank system. However, for the convective mass mode, it can be notice that increasing the depth of the liquefied soil deposit slightly decrease the natural period since the convective mass system was already more flexible due to the presence of springs attaching the mass to the wall, in contrast to the rigid connection between the impulsive mass and the tank wall.

4.2 Nonlinear time history results

The seismic analyses for the LNG tank on the different sub soil scenarios as shown in Fig. 2 were conducted in time domain for two spectral matched earthquake records, namely, the 1999 Chi-Chi and the 1968 Hachinohe earthquakes. The seismic results were extracted and compared in terms of the response spectrum, tanks maximum acceleration profile, inner tank wall maximum structural response, and the pile seismic response (i.e. lateral displacements, shear forces and bending moments developed along the pile).

4.2.1 Response spectrum

Figure 16 displays the acceleration response spectra at the ground surface (i.e. the raft level of LNG tank) for four soil deposit scenarios with different depth of liquefied soil. The induced motion in the soil gets modified as it propagates through the soil deposit from the bedrock level to ground surface, which is known as the site effect. The extent of the site effect depends on the geometrical and mechanical characteristics of the soil deposit and the applied earthquake. Indeed, Fig. 16a shows the amplification of the 1999 Chi-Chi earthquake input motion from the bedrock to the ground surface for the no liquefaction scenario, where the peak ground acceleration (PGA) for the input motion at the bedrock level was 1.85 g and increased to 3.5 g on the ground surface (i.e. almost twice amplification). Similar observations could be made in Fig. 16b for the 1968 Hachinohe earthquake where the PGA amplified from 1.95 g (bedrock level) to 4.1 g (ground surface level). However, the acceleration response spectra decreased when the soil liquefaction occurred, as a result of energy dissipation within the liquefied soil layer. As also evident in Fig. 16, increasing the thickness of the liquefied soil layer from 5.0 to 15.0 m incrementally resulted in continuous increase in the dissipation of the seismic wave as evident in the corresponding reduction in the PGA measured on the ground surface. However, the presence of liquefied soil deposit amplified the spectral acceleration in the long period rang and shifted the peak response spectrum towards the long period rang. These observations are comparable with the results reported by Youd and Carter (2005) and Gingery et al. (2015). Indeed, Youd and Carter (2005) studied five real liquefied sites and found that the liquefaction induced

Fig. 15 The deformation value (U) of the fundamental vibration mode shape for LNG tank with different soil deposit condition: **a** LNG tank on end-bearing piled foundation with non-liquefied soil deposit, **b** LNG tank on end-bearing piled foundation with 5.0 m liquefied soil deposit, and **c** LNG tank on end-bearing piled foundation with 10.0 m liquefied soil deposit, **d** LNG tank on end-bearing piled foundation with 15.0 m liquefied soil deposit ▶

softening reduced the spectral acceleration in the short period (i.e. period range less than 1.0 s), while in long period range (i.e. period range more than 1.0 s), the amplification of the spectral acceleration was observed due to the ground oscillations in this range. Referring to Fig. 16, it can be observed when the thickness of the liquefied soil increased, the extent of soil softening was more, alerting the vibration characteristics of the soil deposit, filtering the high frequency components of the input motions, and delaying the transition of the seismic motion to the ground surface.

Figure 17 shows the effect of the liquified soil layer thickness on the frequency content of the seismic input motion. By comparing the frequency corresponding to the maximum Fourier amplitude (f_d), it can be seen that when the thickness of the liquified soil layer increased, f_d decreased. For the 1999 Chi-Chi earthquake, for the liquified soil thickness of 0, 5 m, 10 m, and 15 m, f_d values were 0.224 Hz, 0.204 Hz, 0.189 Hz and 0.181 Hz, respectively, while the corresponding values from the 1968 Hachinohe earthquake were 0.169 Hz, 0.159, 0.131 Hz and 0.125 Hz.

4.2.2 Maximum tank acceleration profile

The profiles of the seismic acceleration developed along the inner and outer tank walls are reported in Figs. 19 and 20, respectively, where the acceleration profile was extracted along the tank wall when the maximum acceleration occurred at the top of the tank walls in X direction (i.e. at polar coordinate where $\theta = 0^\circ$ and parallel to the direction of applied earthquake). Figure 18 shows the horizontal acceleration time history record of the outer tank roof for different soil conditions. It is evident that the maximum horizontal acceleration occurred at different times for each soil condition scenario under same earthquake; for example, for non-liquefied soil deposit, the maximum horizontal acceleration was observed at t = 6.0 s and t = 7.4 s under the 1999 Chi-Chi and the 1968 Hachinohe earthquakes, respectively. However, the maximum horizontal accelerations were observed at t = 6.2 s, 7.5 s and 7.8 s when the liquefied soil deposit increased to 5.0 m, 10 and 15.0 m under the 1999 Chi-Chi earthquake (Fig. 18a). The corresponding values under the 1968 Hachinohe earthquake were t = 7.8 s, 8.3 s, and 10.8 s, respectively (Fig. 18b). This can be explained by referring to the Fig. 16 where the liquefied soil layer changed the amplitude and frequency content of the seismic load. Referring to Fig. 19a and as expected, the maximum acceleration profile was observed in non-liquefied soil case (i.e. Scenario I), where the maximum recorded acceleration at the top of the outer tank wall was 2.3 g, and decreases gradually to 1.62 g, 0.98 g and 0.92 g in the presence of 5.0 m (Scenario II), 10.0 m (Scenario III) and 15.0 m (Scenario IV) thick liquefied soil deposit, respectively. Similarly, Fig. 19b shows the maximum acceleration of the outer tank wall under the effect of the 1968 Hachinohe earthquake, where the maximum acceleration values of 1.83 g, 1.78 g, 0.82 g, and 0.52 g were observed for Scenarios I to IV, respectively.

Figure 20 shows the maximum acceleration for the inner steel tank wall under the 1999 Chi-Chi (Fig. 20a) and the 1968 Hachinohe (Fig. 20b) earthquakes. As evident, the acceleration along the inner tank wall experienced significant fluctuations in Z direction (i.e. tank wall elevation highlighting the impacts of seismic fluid – structure interaction

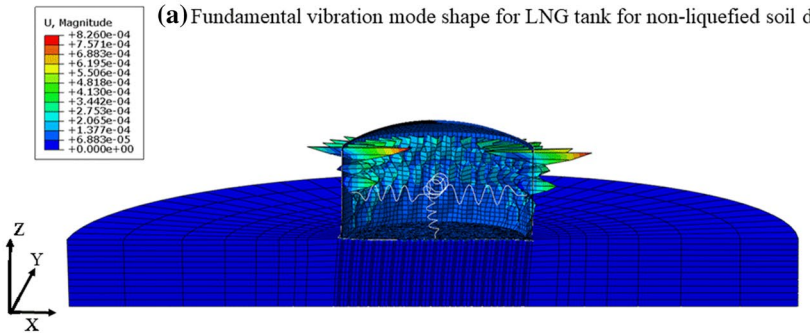

(a) Fundamental vibration mode shape for LNG tank for non-liquefied soil deposit.

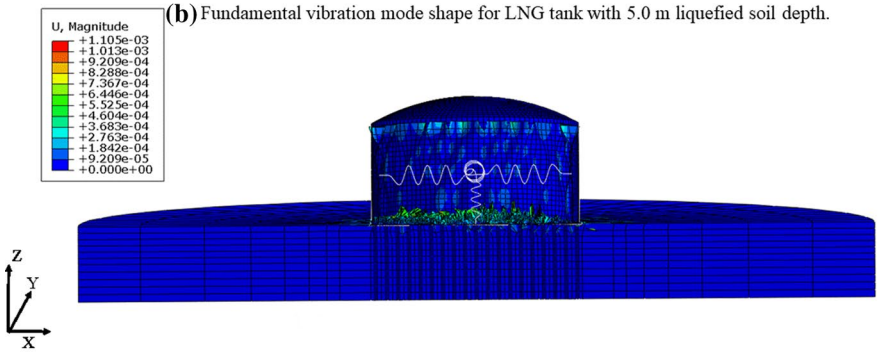

(b) Fundamental vibration mode shape for LNG tank with 5.0 m liquefied soil depth.

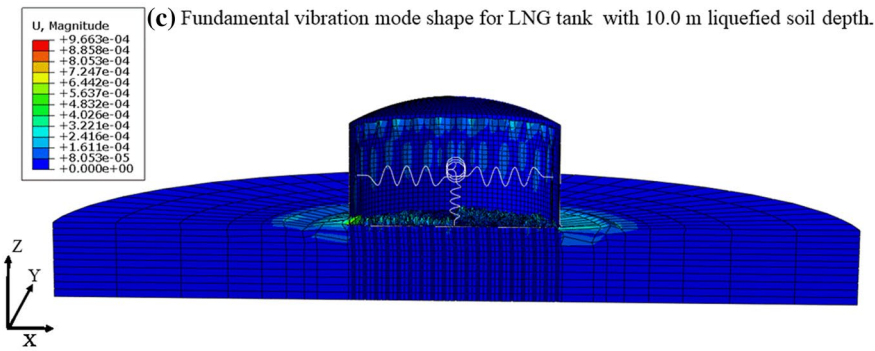

(c) Fundamental vibration mode shape for LNG tank with 10.0 m liquefied soil depth.

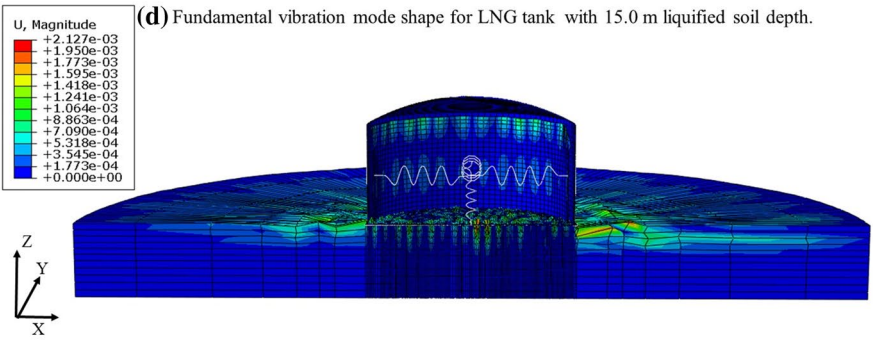

(d) Fundamental vibration mode shape for LNG tank with 15.0 m liquified soil depth.

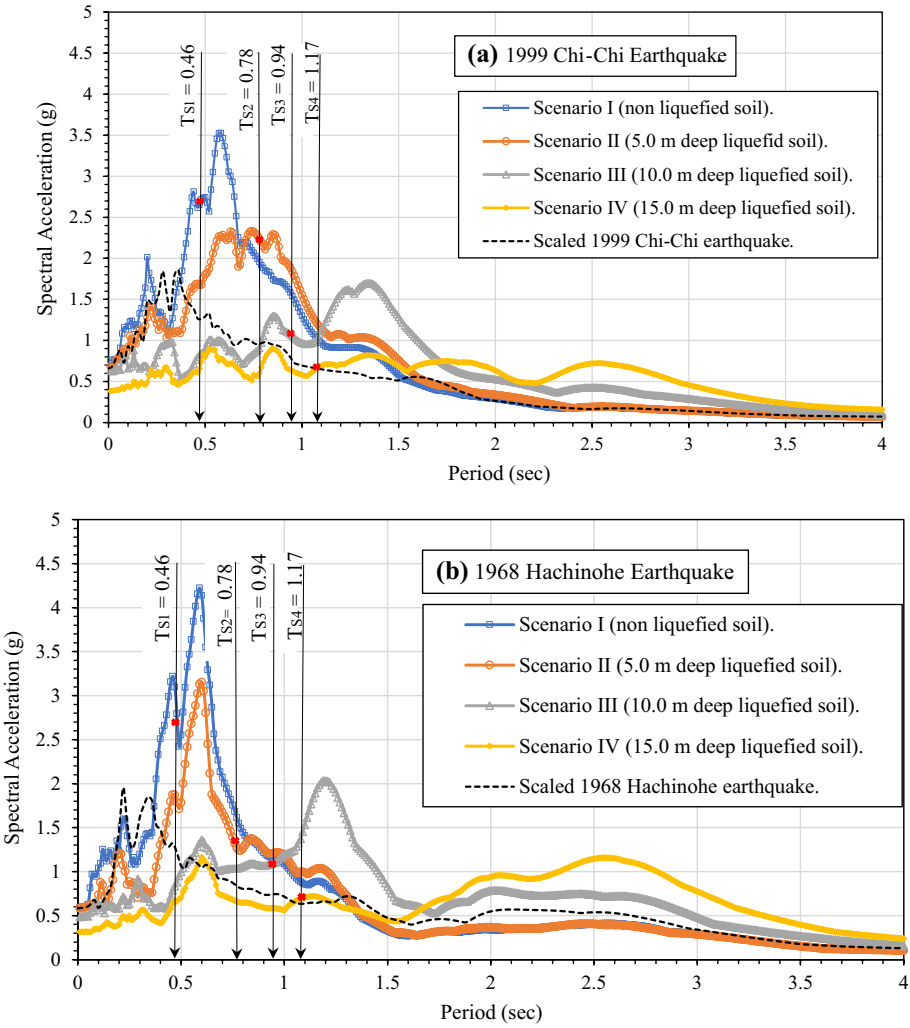

Fig. 16 Response spectrum derived from the motion of foundation slab with 5% damping ratio under **a** 1999 Chi-Chi Earthquake, and **b** 1968 Hachinohe Earthquake

(FSI) as a result of impulsive and convective hydrodynamic forces applied on the tank wall. For both earthquakes, presence of thicker liquefied soil deposit reduced the seismic acceleration induced at the tank base, as well as along the tank wall. Besides, it can be seen that at the location where the convective mass was connected to the wall (i.e. H = 20.0 m), the peak acceleration for the LNG tank under Scenarios III and IV behaved quite differently to Scenario I and II, as the horizontal acceleration increased at convective mass level when the soil liquefied, while an opposite trend was observed for the non-liquefied soil deposit. Indeed, as the liquefied soil thickness increased, the frequency of the seismic load experience by the inner tank decreased, contributing to the increase in the convective mass acceleration, similar to observations made by Kianoush and Ghaemmaghami (2011).

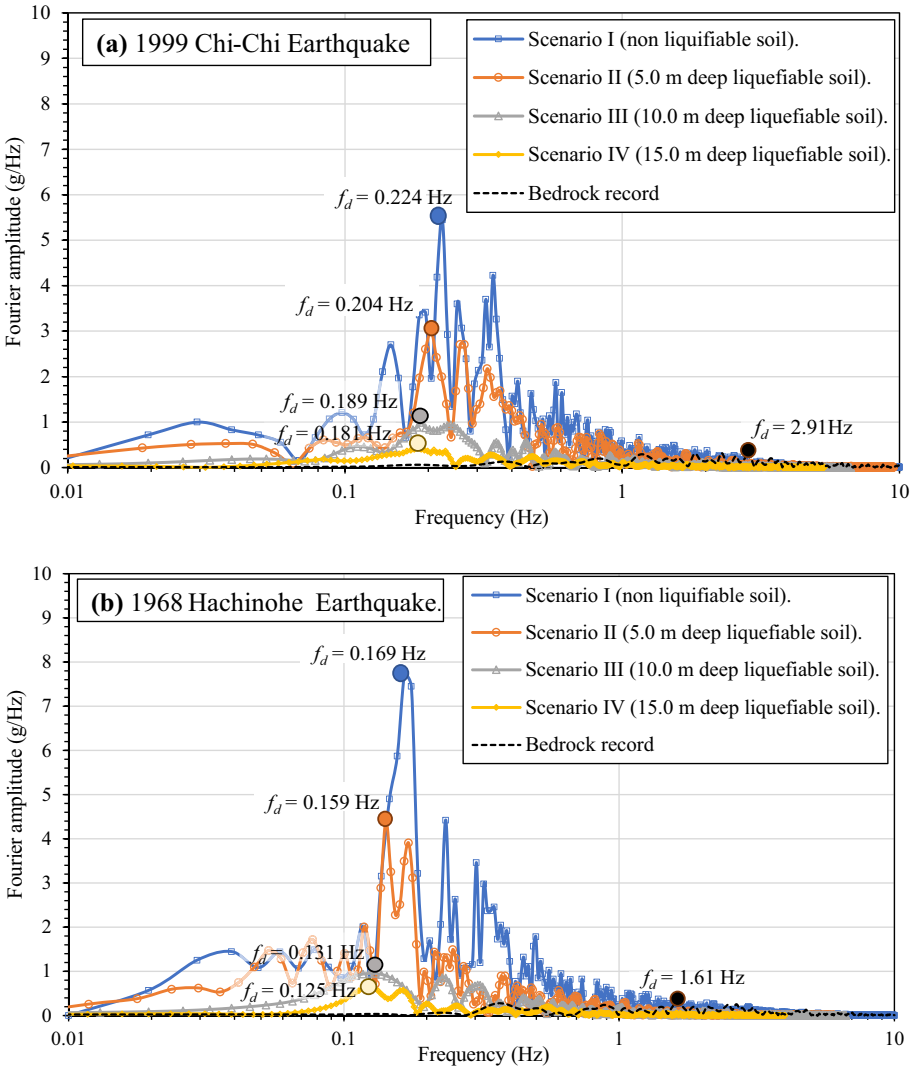

Fig. 17 Corresponding Fourier spectrum at the ground surface level for different liquified soil deposit depths **a** 1999 Chi-Chi Earthquake, and **b** 1968 Hachinohe Earthquake

4.2.3 The structural response of the LNG tanks

The maximum structural response of the inner steel tank under the applied earthquakes in terms of generated forces and displacements along the tank wall are reported and discussed in this section. Assessing the impacts of the soil liquefaction surrounding the piles on the resilience of the steel tank against different failure modes is very crucial. Indeed, the hydrodynamic forces applied to the inner tank as a result of earthquake result in amplified hoop and axial forces in the steel tank wall and potentially cause the inner tank shell buckling. In fact, the shell buckling is the main failure mode for ground

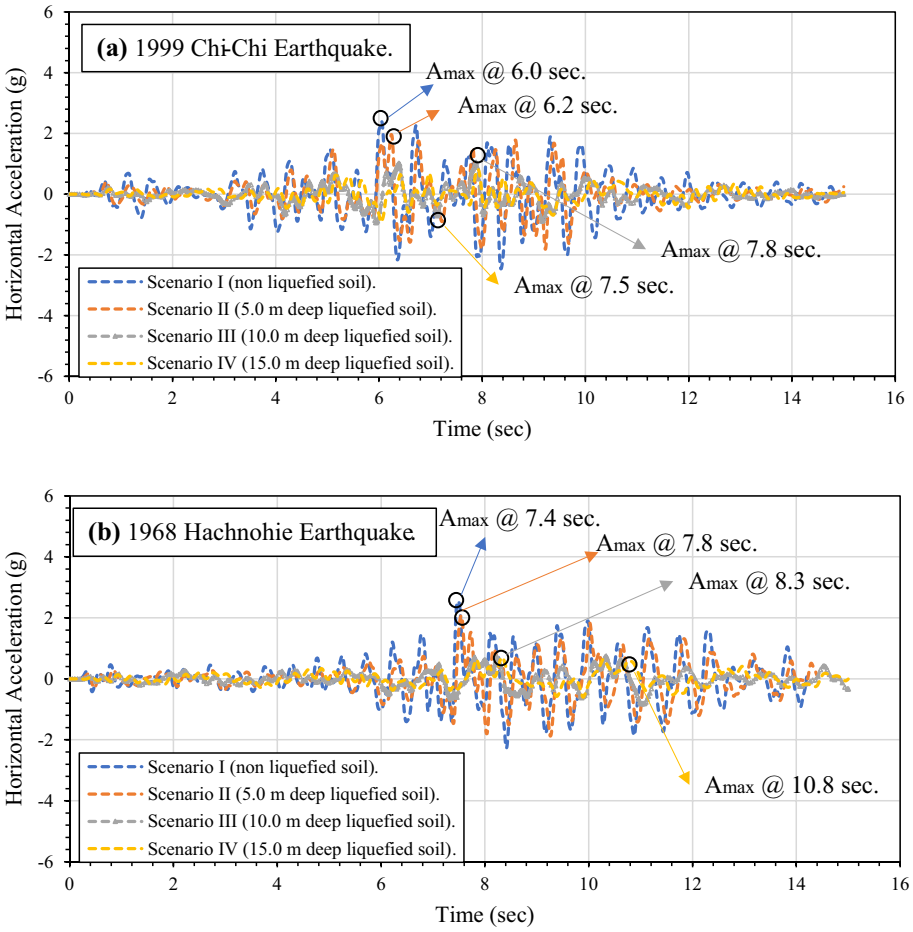

Fig. 18 Horizontal acceleration record of outer tank roof for different foundation options subjected to **a** 1999 Chi-Chi Earthquake, and **b** 1968 Hachinohe Earthquake

supported steel tanks (Brunesi et al. 2015; Dogangun et al. 2009). The failure of steel tanks subjected to the hydrodynamic forces, can be due to elastic or elastoplastic buckling. The elastoplastic buckling occurs when the axial compression and the circumferential hoop stresses (due to the self-weight and hydrostatic and hydrodynamic pressures) exceed the yield limit, often near the based on the tank, and result in an outward bulge appearing which is known as elephant's foot buckling mode. The diamond-shaped buckling mode, which is an elastic buckling often happens at small values of hoop stresses, where inward hydrodynamic suction at the base level of the tank wall or at upper level of the tank wall (corresponding to secondary diamond shape buckling mode) exceed the outward hydrostatic pressure. Indeed, the distribution of the hydrodynamic forces along the tank wall plays a critical role in formation of diamond-shaped buckling, even if stresses remain in the elastic range. Thus, the axial force (F_{11}) and the hoop force (F_{22}) for circumferential unit width of the tank and radial displacements of the inner tank wall are presented and discussed for various foundation conditions.

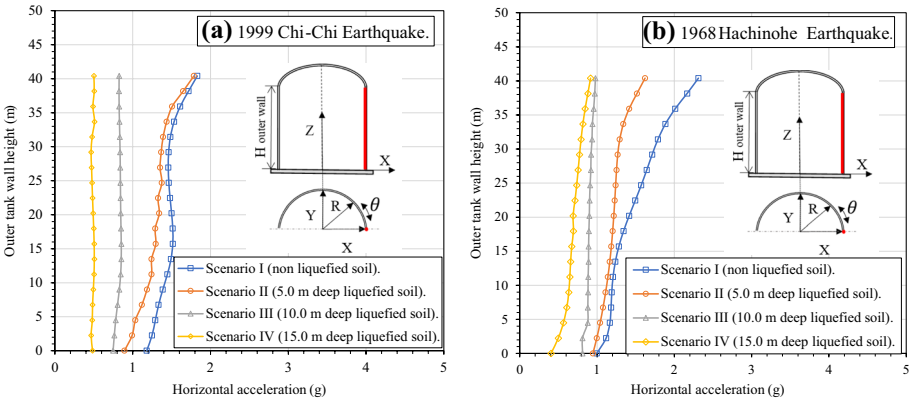

Fig. 19 Maximum horizontal acceleration profile along outer tank wall for different foundation options subjected to **a** 1999 Chi-Chi Earthquake, and **b** 1968 Hachinohe Earthquake

Figure 21 shows the time history of the horizontal displacement of the inner tank top, indicating that the maximum lateral displacements of the inner tank were observed at different times for different soil deposit scenarios. Figure 21a indicates that the maximum horizontal displacement of the inner tank under 1999 Chi-Chi earthquake occurred at t = 9.4 s, 9.3 s, 10.0 s and 10.4 s, for Scenarios IV, III, II, and I, respectively. The corresponding value under the 1968 Hachinohe earthquake were t = 11.0 s, 10.1 s, 10.0 s and 13.0 s, respectively (Fig. 21b). It can be noticed that increasing the thickness of the liquefiable soil deposit increased the lateral displacement amplitude and the maximum lateral deformation of the superstructure.

Figure 22 shows the distribution of the hoop forces (F_{22}) within the inner tank shell under 1999 Chi-Chi and 1968 Hachinohe earthquakes when the maximum deformation of the tank was recorded. The distribution of the hoop forces along the inner steel tank wall is in a line with the horizontal accelerations recorded for the inner steel tank wall (see Fig. 20). The maximum hoop forces in the upper portion of the tank wall for the soil deposit Scenarios I and II, exceeded those of Scenarios III and IV. Indeed, since the impulsive mode periods for Scenarios I and II (i.e. 0.51 s and 0.78 s as in Table 7), were located in the shorter period range of the acceleration response spectrum (Fig. 16), the amplification of seismic forces was observed. However, the lengthened impulsive mode periods for Scenarios III and IV (i.e. 0.94 s and 1.17 s as in Table 7) were located in longer period range with decreased spectral accelerate range, which resulted in reduced the seismic forces due to impulsive mass. It is noticed that the maximum hoop forces for the tank built on non-liquefiable soil deposit subjected to the 1999 Chi-Chi earthquake (refer to Fig. 22a) and the 1968 Hachinohe earthquake (Fig. 22b) were 1.3 MN/m and 2.87 MN/m, respectively.

On the other hand, Fig. 23 shows the maximum axial forces (F_{11}) along the inner tank wall at $\theta = 0^\circ$ for different soil deposits considered (i.e. Scenarios I to IV) when the maximum horizontal displacement of the tank was observed. It is evident that the axial forces in the inner tank generally increased from the top to the bottom along the inner steel tank wall with the maximum observed at $Z/H = 0.10–0.375$ (or $Z/H_L = 0.12–0.44$). In addition, referring to Fig. 23, the maximum axial forces in the inner tank wall decreased with the increasing depth of the liquefied soil. For example, under 1999 Chi-Chi earthquake, when

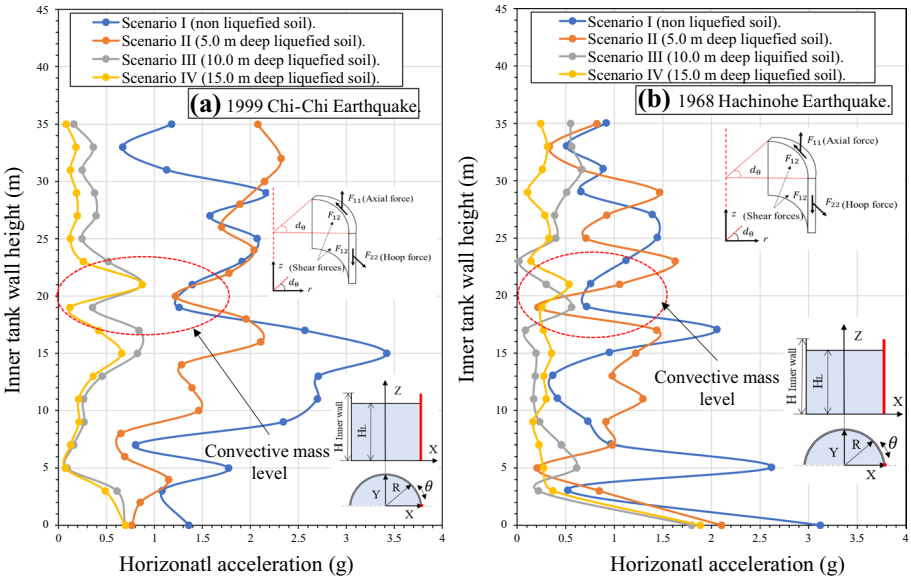

Fig. 20 Maximum horizontal acceleration profile along Inner tank wall for different foundation options subjected to **a** 1999 Chi-Chi Earthquake, and **b** 1968 Hachinohe Earthquake

the depth of liquefied soil was increased from zero to 5.0 m, the axial force reduced by 21%, and increasing the depth of liquefied soil layer to 10.0 m and 15.0 m reduced the axial force by 42% and 50%, respectively (Fig. 23a).

Figure 24 captures the distribution of the shear forces along the inner steel tank wall when the maximum lateral displacement was observed (as indicated in Fig. 21). It is evident that for both earthquakes, the maximum shear forces were observed at the base of the inner tank wall where the maximum axial forces were reported. Moreover, a second local peak of the shear force was recorded near the middle of the tank wall (i.e. $Z/H = 0.45$ or $Z/H_L = 0.52$ in the vicinity of the location where the convective mass was attached to the wall, at which significant variation of the hoop forces were also reported. As evident in Fig. 24, among the soil deposit scenarios considered, the non-liquefiable soil deposit (Scenario I) resulted in the maximum mobilised shear forces in the inner tank under both earthquakes.

Figure 25 shows the radial displacements along the inner tank wall when the maximum lateral displacement was reported (as indicated in Fig. 21). It is evident that the most significant radial displacement gradient (or section rotation) was observed in vicinity of the mid-height of the inner tank, where the second peak of the shear forces were observed. Indeed, the convective hydrodynamic force applied at the mid height of the inner tank wall could alert the structural response of the inner tank. As discussed earlier, increasing the liquefied soil depth resulted in changing the seismic waves, mainly by reducing the frequency, resulting in the reduction in the impulsive forces, and in contrary amplification of the convective forces. This observation highlights the importance of including the convective mass in the seismic analysis of the LNG tanks, especially, where the presence of the liquefiable soil deposit can increase the flexibility and natural period of the soil-structure system significantly. This can result in amplified

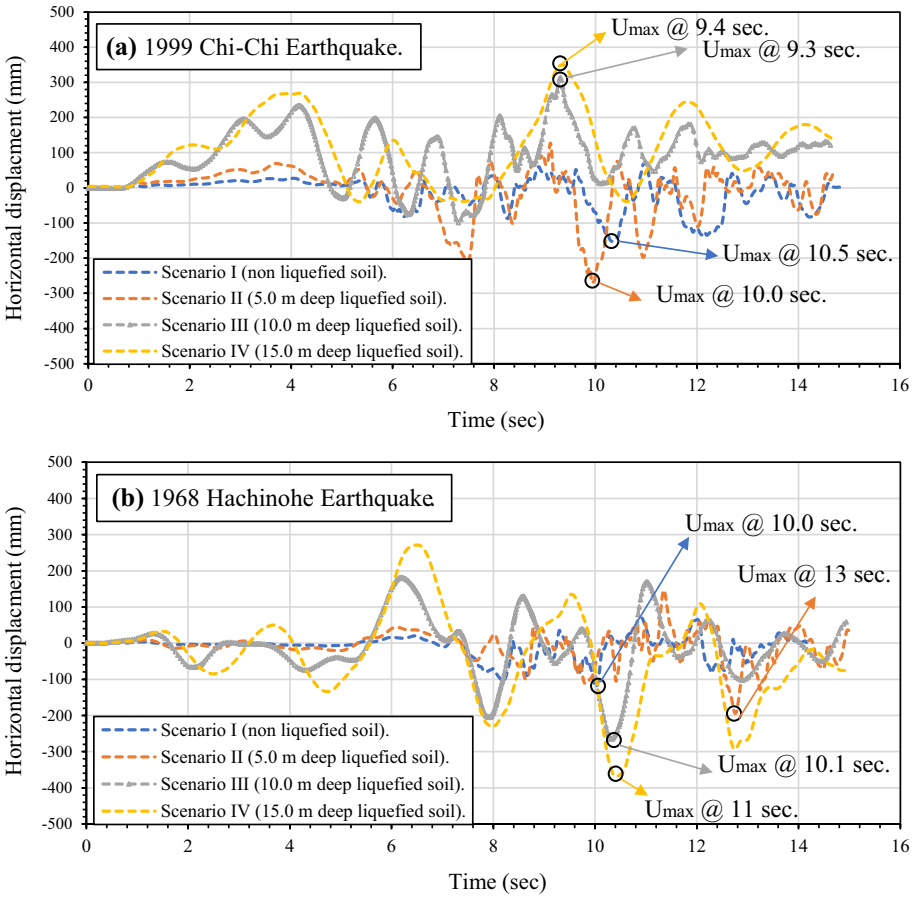

Fig. 21 Horizontal displacement record of Inner tank top for different foundation options subjected to **a** 1999 Chi-Chi Earthquake, and **b** 1968 Hachinohe Earthquake

radial displacement of the LNG tank system which can in turn introduce more convective hydrodynamic forces to the system.

Figure 26 presents the maximum Von Mises stresses generated in the inner tank wall under the 1999 Chi-Chi (Fig. 26a) and the 1968 Hachinohe (Fig. 26b) earthquakes. The results show that the maximum induced Von Mises stresses corresponded to the LNG tank built on the non-liquefiable soil deposit (i.e. Scenario I) for both earthquakes, where the maximum induced plastic strains reached 0.29% and 0.89% for the 1999 Chi-Chi earthquake (Fig. 27a) and the 1968 Hachinohe (Fig. 27b) earthquakes, respectively. The above observations show that for the LNG tank on the non-liquefiable soil deposit, elastic–plastic buckling may happen in the upper section of the tank where plastic deformations are observed as a result of the von Mises stresses exceeding the yield stress. However, when soil liquefaction occurs, due to period lengthening and significant soil damping, stresses in the inner tank may reduce below the yield limit, while more concentrated stresses may be observed in the lower section of the tank near the base, where potential elephant foot buckling failure may occur.

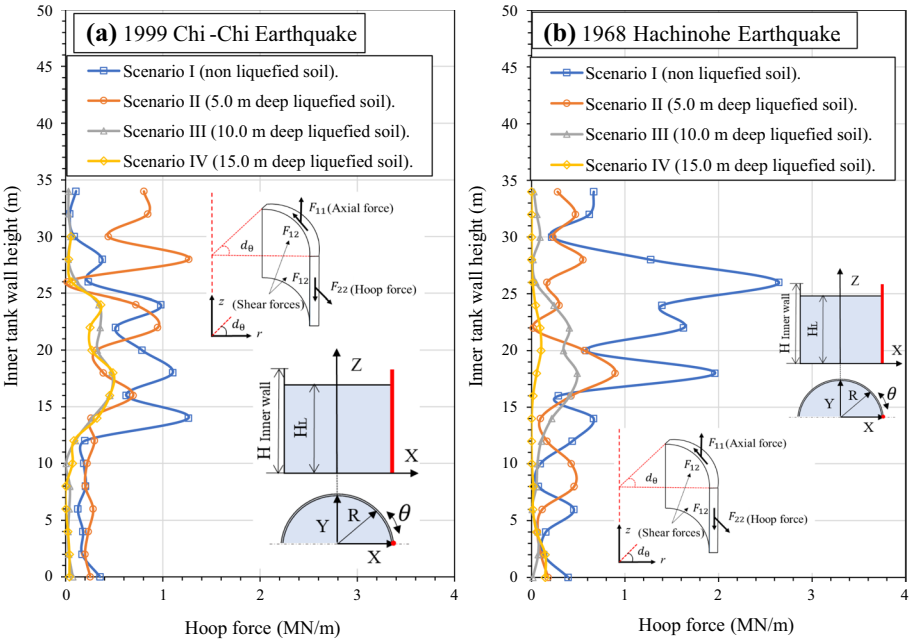

Fig. 22 Distribution of the hoop forces in the tank wall at $\theta = 0^{\circ}$: to **a** 1999 Chi-Chi Earthquake, and **b** 1968 Hachinohe earthquake

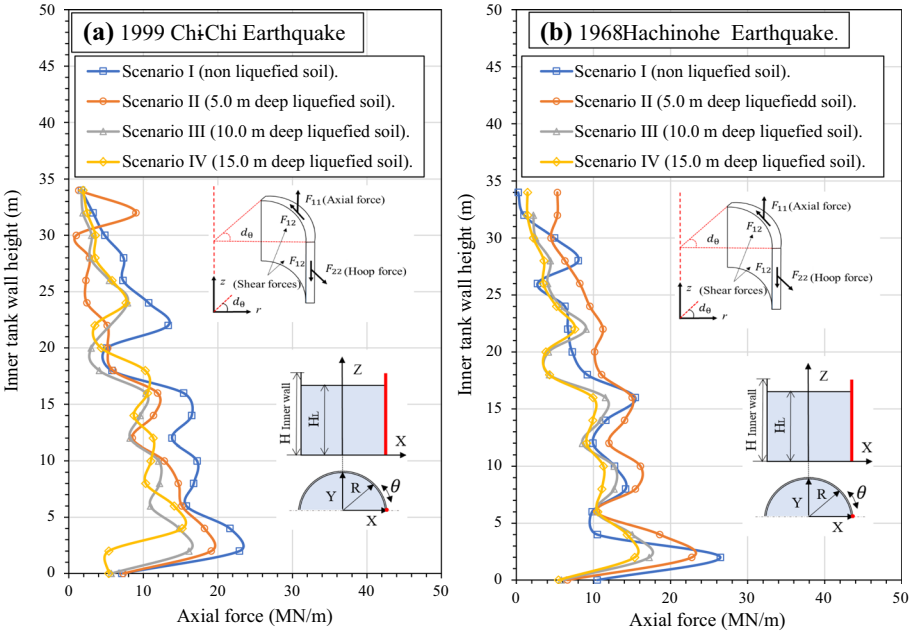

Fig. 23 Distribution of the axial forces in the inner tank wall at $\theta = 0^{\circ}$: to **a** 1999 Chi-Chi Earthquake, and **b** 1968 Hachinohe earthquake

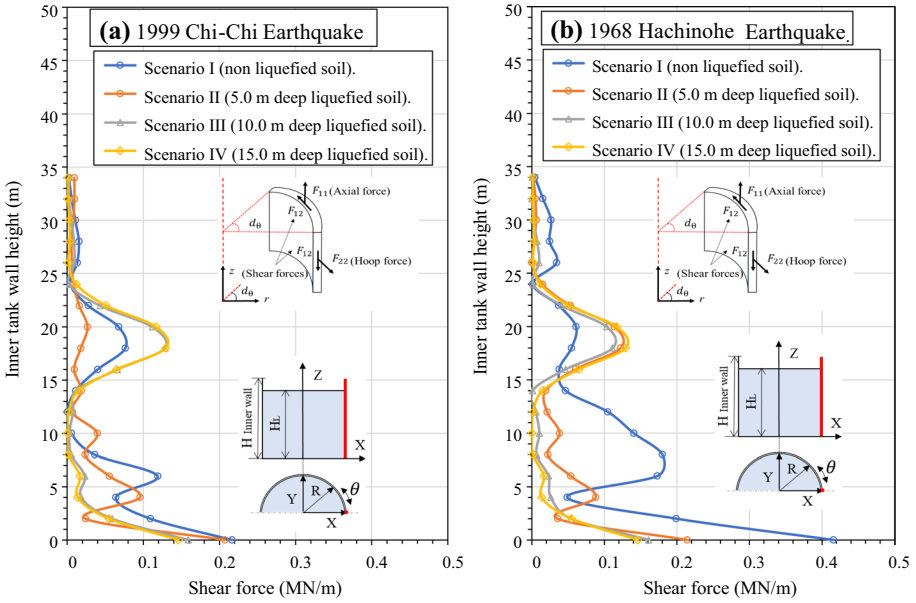

Fig. 24 Distribution of the shear forces in the inner tank wall at $\theta = 0^{\circ}$: to **a** 1999 Chi-Chi Earthquake, and **b** 1968 Hachinohe earthquake

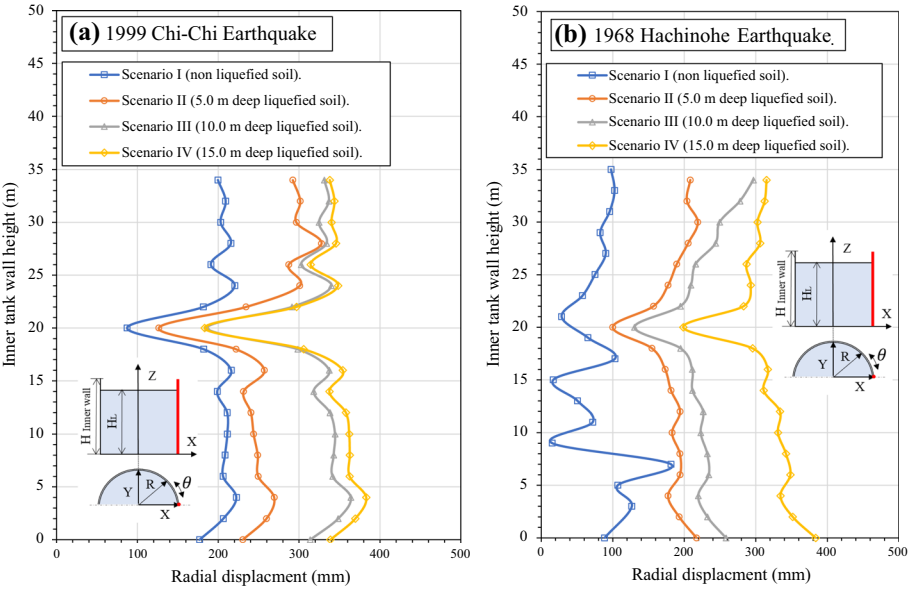

Fig. 25 Distribution of the Radial displacement *in* the inner tank wall at $\theta = 0^{\circ}$: to **a** 1999 Chi-Chi Earthquake, and **b** 1968 Hachinohe earthquake

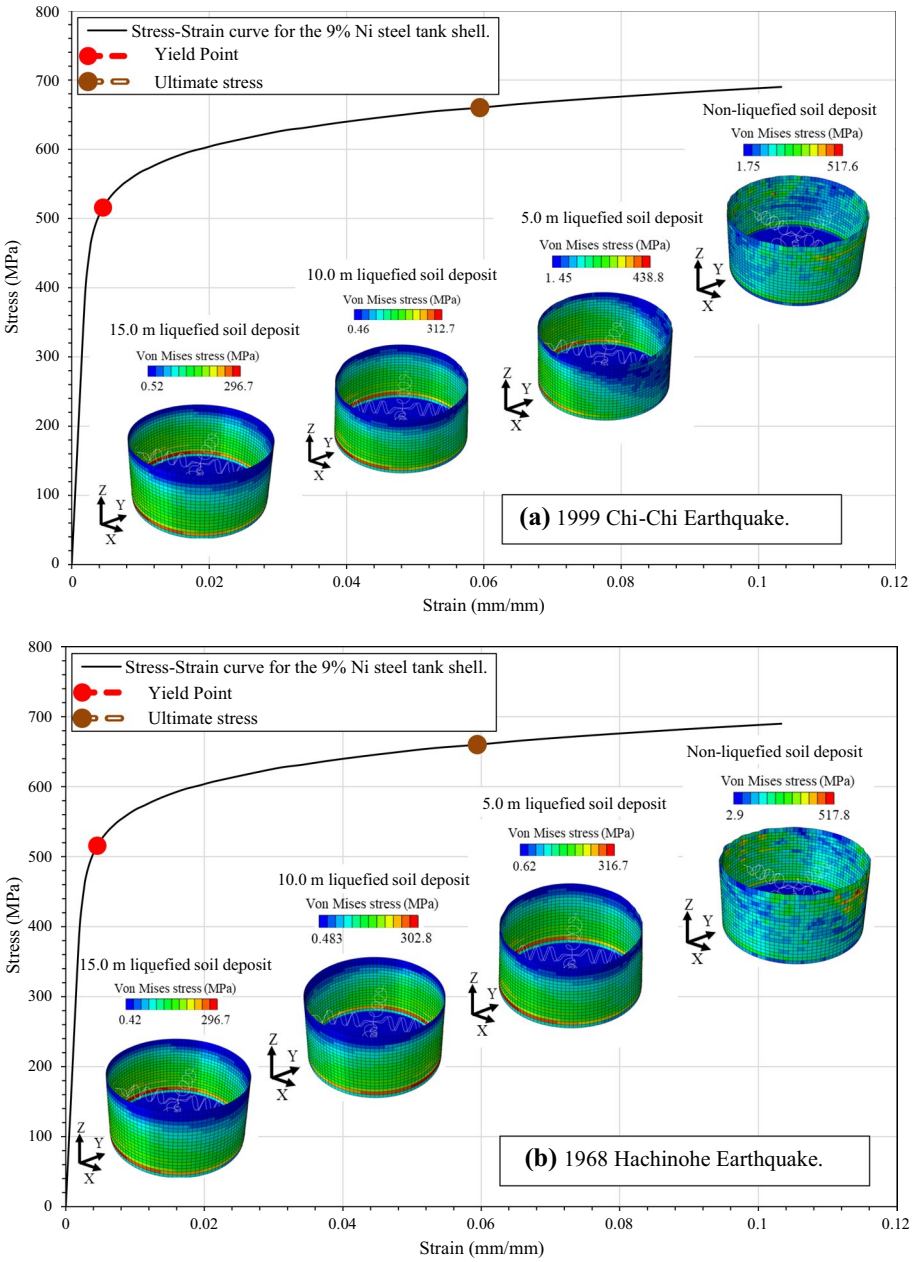

Fig. 26 The maximum von Mises stress on the inner 9% Ni steel tank wall and the location of the maximum stress on the stress- strain under **a** 1999 Chi-Chi Earthquake, **b** 1968 Hachinohe earthquake

Figures 28 and 29 present the maximum von Mises stresses generated in the outer tank wall under the 1999 Chi-Chi and the 1968 Hachinohe earthquakes, respectively. It should be mentioned here that since no failure was observed in the inner tank under any analysed

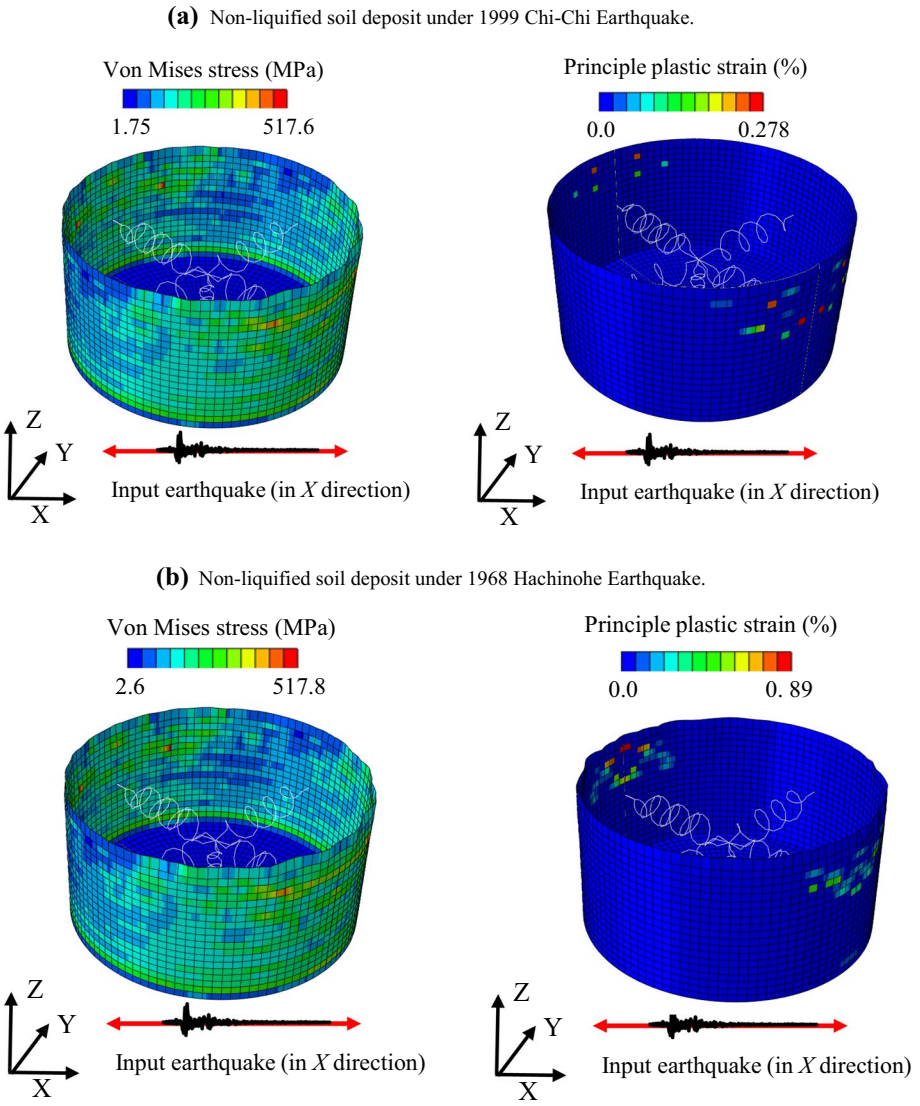

Fig. 27 The maximum von Mises stress on the inner 9% Ni steel tank wall and the corresponding plastic strain at the end of the earthquake of **a** 1999 Chi-Chi Earthquake, **b** 1968 Hachinohe Earthquake

scenarios, no leakage of LNG from the inner tank was considered, and thus LNG was not in the direct contact with the outer tank wall in this study. It is evident that the non-liquefied soil deposit scenario (Scenario I) led to the maximum generated von Mises stresses in the outer tank wall. According to Fig. 28, the maximum von Mises stress decreased from 25.9 MPa to 19.9 MPa when the top 5.0 m of soil deposit had liquefied under 1999 Chi- Chi earthquake, while when the liquefied soil layer extended to 10.0 m and 15.0 m, the maximum von Mises stresses reduced to 18.4 MPa and 10.9 MPa respectively. It can be seen that the maximum stresses in the outer tank were generated at the connection

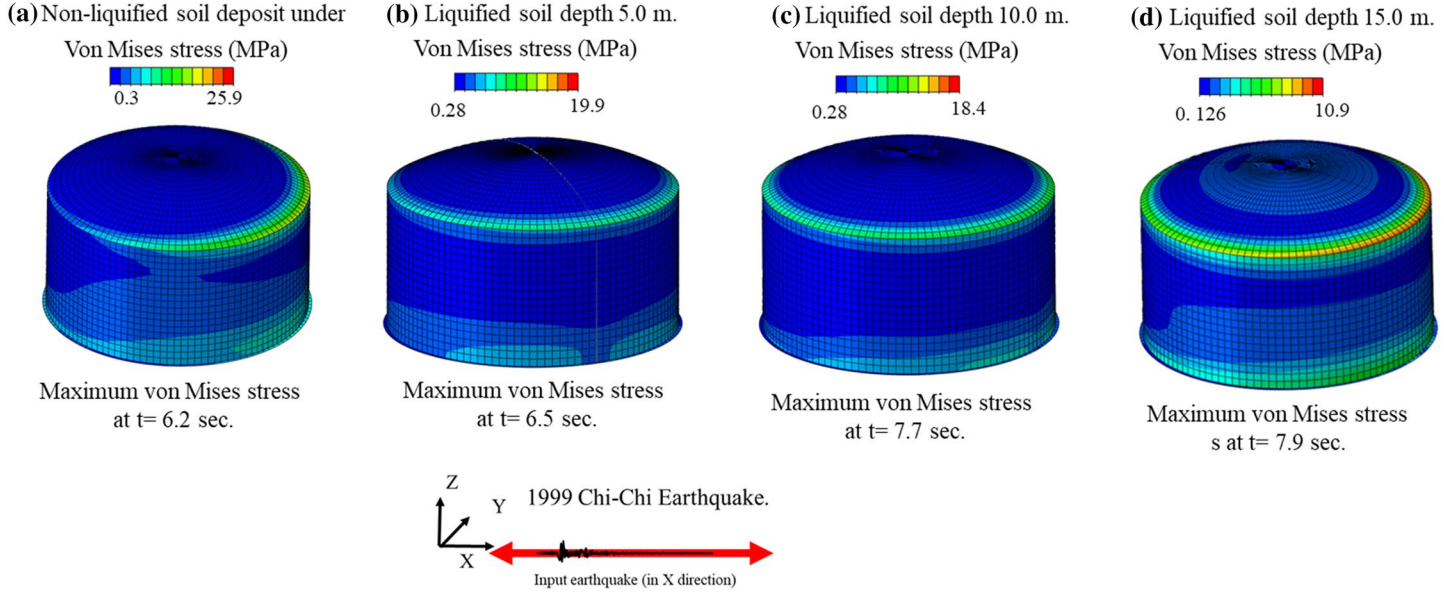

Fig. 28 The maximum von Mises stress on outer concrete tank under the effect of 1999 Chi-Chi Earthquake for different soil deposit scenarios namely, **a** non-liquified soil deposit, **b** 5.0 m liquified soil depth, **c** 10.0 m liquified soil depth and **d** 15.0 m liquified soil depth

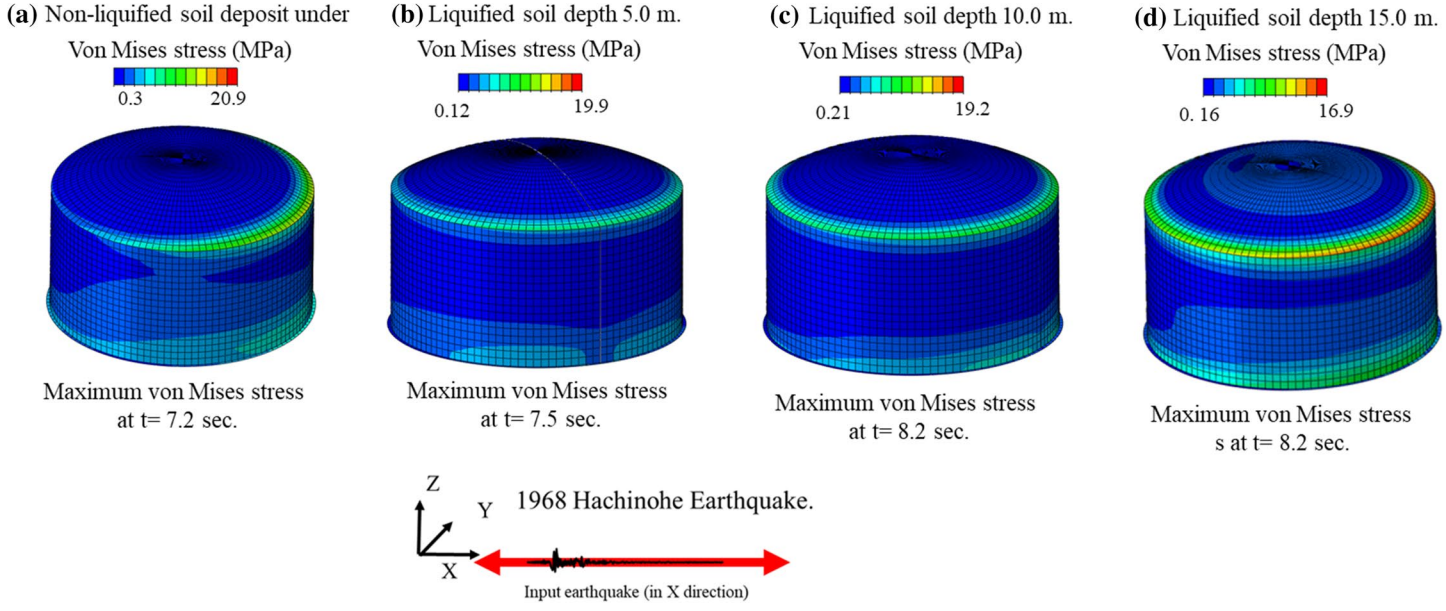

Fig. 29 The maximum von Mises stress on outer concrete tank under the effect of 1968 Hachinohe Earthquake for different soil deposit scenarios namely, **a** non-liquified soil deposit, **b** 5.0 m liquified soil depth, **c** 10.0 m liquified soil depth and **d** 15.0 m l

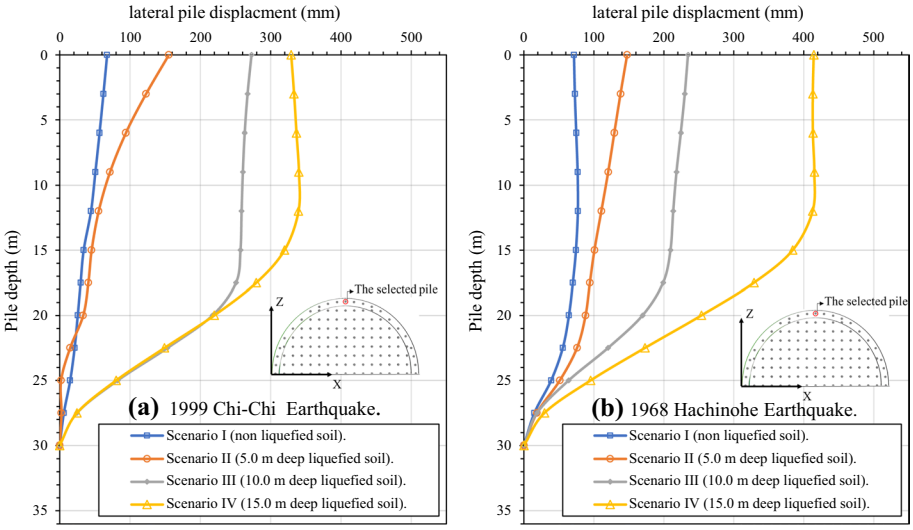

Fig. 30 Maximum lateral pile displacement for different soil deposit scenarios along the pile length subjected to **a** 1999 Chi-Chi Earthquake, **b** 1968 Hachinohe earthquake

between the tank wall and the roof for both earthquakes. Moreover, referring to Fig. 29, the maximum von Mises stresses decreased by 5%, 4% and 19% when the liquefied soil depth increased from zero to 5.0 m, 10.0 m and 15.0 m respectively. These results are in a line with the maximum acceleration reported for the outer tank as in Figs. 18 and 19.

4.2.4 Seismic response of pile foundation

To investigate the effects of liquefiable soil deposit on the response of piles supporting the LNG tank, the pile in the outermost ring of piles in *Y* direction as shown in Fig. 30 was selected. This pile was selected because it is under the outer tank wall and resists the highest shear forces, lateral displacement and overturning effects (Tajirian et al. 2019). Referring to Figs. 30, 31 and 32, the lateral displacement, shear force, and bending moment profiles along the pile length were reported when the maximum response (i.e. displacement) at the pile head was observed.

Referring to Fig. 30, as the liquefied soil depth increased, the lateral pile displacement also increased. Indeed, since the liquefied soil layer lost the stiffness and shear strength significantly, the ground displaced more laterally and piles experienced larger deflections. According to Fig. 30a, the maximum lateral deflection of the pile head increased from 72 to 150 mm, 272 mm and 330 mm when the liquefiable soil depth increased from 0 (non-liquefiable soils deposit Scenario I) to 5.0 m (Scenario II), 10.0 m (Scenario III), and 15.0 m (Scenario IV) under the 1999 Chi-Chi earthquake, respectively. The corresponding lateral displacements for the 1968 Hachinohe earthquake were 80 mm (Scenario I), 155 mm (Scenario II), 243 mm (Scenario III) and 410 mm (Scenario IV), respectively (see Fig. 30b).

Figures 31 and 32 show the shear force and bending moment envelopes along the pile length. In general, once the seismic wave affected the superstructure, the inertial forces transferred from the superstructure to the pile heads and ultimately to the soil deposit. After the liquefaction occurred, more lateral displacement was developed in the vicinity of

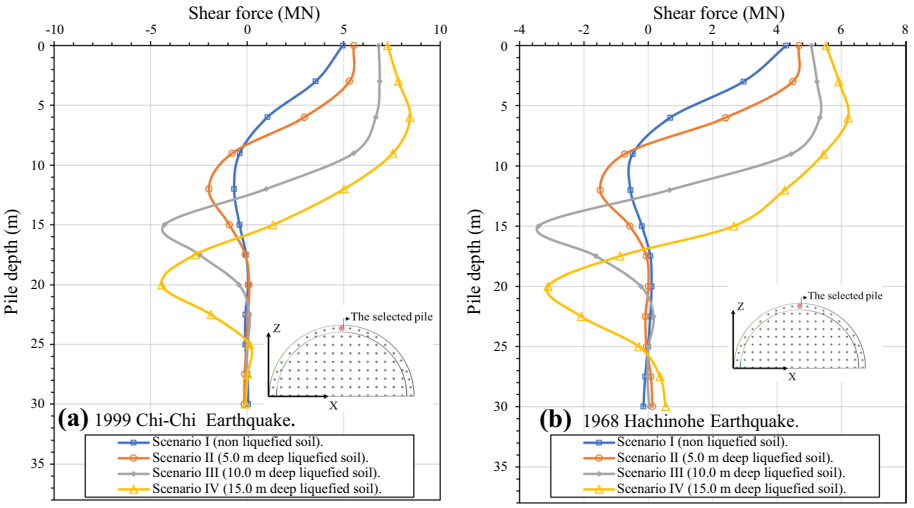

Fig. 31 Maximum shear force profile imposed on the pile for different soil deposit scenarios along the pile length subjected to **a** 1999 Chi-Chi Earthquake, **b** 1968 Hachinohe earthquake

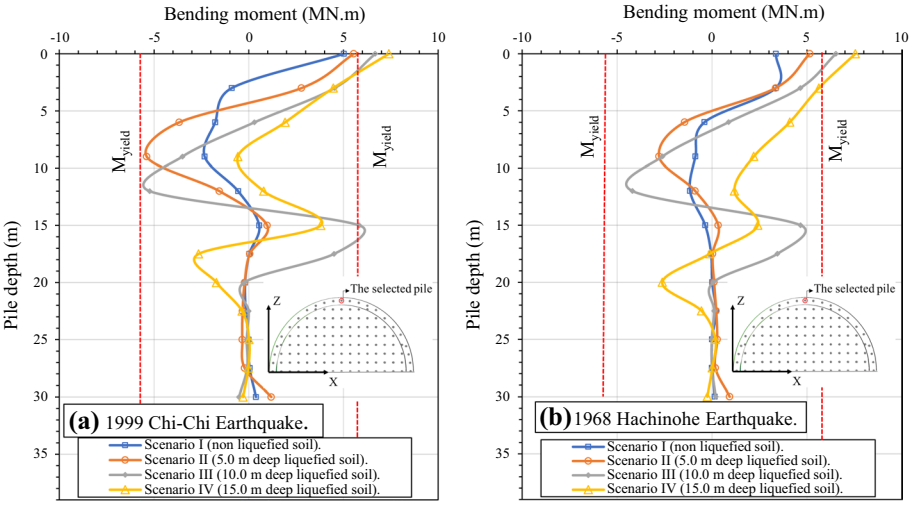

Fig. 32 Maximum bending profile imposed on the pile for different soil deposit scenarios along the pile length subjected to **a** 1999 Chi-Chi Earthquake, **b** 1968 Hachinohe earthquake

the ground surface which induced more bending moments near the top of the piles. Therefore, the piles behaved like rather unsupported column in that section. As the liquefied soil depth increased, the pile head displacement increased and subsequently the shear forces increased as in Fig. 31.

Similar to shear forces, the bending moments generated at the pile head increased as the depth of liquefied soil increased. As Fig. 32 shows, in Scenario I, where the soil deposit was non-liquefiable, the maximum bending moment was observed at the pile head, while

for other scenarios where soil liquefaction occurred, local amplified bending moments were observed well below the ground surface. In addition, the higher values of bending moment and shear forces were observed at the boundary between the liquefied and non-liquefied soil layers where abrupt the soil stiffness change was observed. These results are comparable with observations made by Rostami et al. (2017) and Dobry et al. (2003) where plastic hinges were generated in the piles at the interfaces between the liquefied and non-liquefied soil layers. However, for heavy superstructure such as LNG tanks, the maximum bending moments are expected to occur at the pile head due to the large inertial forces, which could exceed the bending moments observed at the boundary between the liquefied soil layer and non-liquefied soil layer. In this study when over one third of the entire soil was liquefied soil (i.e. Scenarios III and IV), the bending moments in the pile exceeded the yield stress. For example, as shown in Fig. 32, the generated bending moments in the piles for Scenario III were 6.6 MN.m (1999 Chi-Chi earthquake) and 6.5 MN.m (1968 Hachinohe earthquake) which exceeded the yield moment of pile $M_{yield} = 5.8$ MN.m, resulting in formation of plastic hinges in the piles. Similarly, the corresponding bending moment generated at the pile head for Scenario IV for both earthquakes reached the ultimate moment capacity of the pile $M_{ultimate} = 7.5$ MN.m resulting in the bending failure of the piles.

The variations of soil stiffness and strength with depth can impact the inertial and kinematic interactions influencing the seismic response of piles (Gazetas and Dobry 1984; Nikolaou et al. 2001) and resulted reported in Figs. 30, 31 and 32 illustrate these effects for pile foundation used in this study. The observed inertial interaction stemmed from the movement of the superstructure generating large shear forces and bending moments in the top part of the piles due to the rigid connection between piles and pile cap, and the forces decayed rapidly with depth in the case of non-liquefiable soil (Scenario I) as evident in Figs. 31 and 32.

When the soil deposit liquefied (i.e. Scenarios II to IV), although the impact of inertial interaction on piles reduced (i.e. less base shear experienced by the superstructure as shown in Fig. 24), the response of piles in terms of shear forces and bending moments increased in the top part of the piles (see Figs. 31 and 32). This is due to the fact that the kinematic interaction between the piles and the surrounding soil became more significant. Indeed, kinematic interaction is caused by the inability of a foundation to match the deformation of the surrounding soil (Kramer 1996). The presence of liquefied soil layer (Scenarios II to IV) introduced larger difference between the stiffnesses of the piles and the surrounding soil compared to Scenario I. Therefore, the inability of the piles to match the deformation of the surrounding soil was more significant resulting in more kinematic interaction induced loads (i.e. shear forces and bending moments). It can be concluded that when the liquefaction occurred in the shallow depth only, the kinematic interaction had a dominant impact on the pile response over inertial interaction. Indeed, with the increase in the thickness of the liquefied layer, the loads developed in the piles due to kinematic interaction increased and extended deeper, while the loads due to inertial interaction decreased.

It should be mentioned that the soil constitutive model used for the clay deposit was the nonlinear kinematic hardening model, which is capable of capturing the variation of soil stiffness with strain under cyclic loading and the required parameters were calibrated against the exiting data in the literature as in Sun et al. (1988) and reported in Fig. 11. While it is preferred to use none-associated flow rule for the response of the soil subjected to cyclic loading, associated flow rule was adopted as a simplifying assumption for the clay soil in undrained conditions, where soil resistance is pressure-independent (Mucciacciaro and Sica 2018). For the liquefied soil deposit, the elastic—perfectly plastic Mohr–Coulomb soil model with Rayleigh damping coefficients was implemented to capture the post

liquefaction response of the sand. However, more advanced nonlinear soil models can be implemented in future studies for more accurate predictions, such as Yang (2000) constitutive soil model, which can capture nonlinear hardening behaviour with multi yield surfaces as implemented by Zhuang et al. (2015).

In addition, due to the complexity of the model and lack of experimental results available for the full-scale system capturing all components, attempts were made in this study to evaluate suitability of different individual components of the system. However, consideration of different utilities such as pipelines attached to the system, more rigorous simulation of response of liquified soil and fluid–structure interaction with more accurate simulation of slushing are examples of improvement recommended for future studies.

5 Conclusions

This paper presented the results of seismic analysis of a 160,000 m^3 full containment LNG tank considering soil -structure interaction (SSI) and the fluid–structure interaction (FSI) while assessing the impacts of the depth of soil liquefaction on performance of different components of the system. Four different soil deposit scenarios were investigated, namely, non-liquefied soil deposit (Scenario I), and liquefied soil deposit with their liquefied layer depth increasing from 5.0 m (Scenario II) to 10.0 m (Scenario III) and 15.0 m (Scenario IV). A three-dimensional numerical model of the entire tanks, piles and soil system was developed, and the free vibration and time history analyses were conducted adopting fully nonlinear analysis in the time domain. Indeed, direct method of analysis was adopted in which the LNG tank, foundation and soil were simulated and analysed in one step.

The free vibration analyses were performed for the LNG tank using Block Lanczos algorithm, and the results showed that the presence of the liquefied soil significantly alerted the dynamic characteristics of the LNG tank, impacting the seismic performance of the tank system. The ground response analysis showed the liquefied soil layer reduced the spectral acceleration in short period range and amplified the spectral accelerations in the long period range, while increasing the liquefied soil depth lengthened the natural period of the LNG tank.

The nonlinear time history results showed that the seismic forces developed in the inner and outer tank systems reduced as the depth of liquefaction increased. Indeed, increased soil damping and increased structural flexibility directed less seismic forces to LNG tank, and thus the case with non-liquifiable soil deposit resulted in the maximum forces and stresses in the superstructure. The observed potential failure of the inner steel tank was the elastic–plastic buckling mode at the mid-height of the inner tank wall, as the von Mises stresses exceed the yield stress for Scenario I. Since, increasing the depth of the liquefied soil, reduced the seismic response of the superstructure, no damage or failure was observed in the inner steel tank for Scenarios II to IV, while localised Von Mises stress were observed near the base of the tank. However, when the liquefied soil depth increase, the impulsive forces along the tank wall decreased, while amplification of convective forces particularly for Scenarios III and IV were observed, since the dominant frequency of the seismic wave was reduced which in turn induced increased convective forces.

On the other hand, soil liquefaction and its depth impacted the seismic response of the pile foundation adversely, due to the observed amplified shear forces, bending moments and deflections in the piles. Moreover, presence of liquefied soil layer exacerbated the inability of the piles to match the deformation of the surrounding soil, and thus resulted in

more kinematic interaction induced loads (i.e. shear forces and bending moments). Indeed, with the increase in the thickness of the liquefied layer, although the loads due to inertial interaction decreased, the loads developed in the piles due to kinematic interaction increased and extended deeper, and eventually additional localised plastic deformations in the piles were observed at depths well below the pile head.

Acknowledgements The first author would like to acknowledge the support provided by Al-Hussein Bin Talal University during the course of this research.

Funding Open Access funding enabled and organized by CAUL and its Member Institutions. The authors have not disclosed any funding.

Declaration

Conflict of interest The authors have not disclosed any competing interests.

References

ABAQUS (2018) [Computer Software] Dassault Systemes Simulia Corporation, Providence, RI, USA

Abdoun T, Dobry R (2002) Evaluation of pile foundation response to lateral spreading. Soil Dyn Earthq Eng 22:1051–1058

ACI 318-08 (2014) Building code requirements for structural concrete and commentary. International Organization for Standardization: American Concrete Institute, Farmington Hills

Agalianos A, De Coquereaumont OD, Anastasopoulos I (2020) Rigid slab foundation subjected to strike–slip faulting: mechanisms and insights. Géotechnique 70(4):354–373

Aggen G, Allen M (2018) Properties and selection: Irons, Steels, and High-Performance Alloys. ASM International: ASM Handbook, vol 1. The materials information company. Novelty, OH, USA

Anastasopoulos I, Kourkoulis R, Gazetas G, Tsatsis A (2013) Interaction of piled foundation with a rupturing normal fault. Géotechnique 63:1042–1059

Animah I, Shafiee M (2020) Application of risk analysis in the liquefied natural gas (LNG) sector: an overview. J Loss Prev Process Ind 63:103–980

API-650 (2007) Welded steel tanks for oil storage. American Petroleum Institute (API) Publishing Services, Eleventh Ed, Washington D.C.

Armstrong PJ, Frederick CO (1966) A mathematical representation of the multiaxial Bauschinger effect, Central Electricity Generating Board and Berkeley Nuclear Laboratories. Research and Development Department, Vol (731)

AS/NZS1170.5 (2004) Standards New Zealand. Structural design actions, Part 5: earthquake actions New Zealand. Wellington

Asimaki D, Garcia-Suarez J, Kusanovic D, Nguyen K, Seylabi EE (2019) Next generation reduced order models for soil-structure interaction. Earthq Geotech Eng Prot Dev Environ Constr 4:138–152

Asran A, Al-esnawy H, Fayed S (2016) A review on reinforced concrete beam-column connections. In: The International Conference on Civil and Architecture Engineering. Military Technical College pp 1–27

ASTM A353 (2014) Standard specific cation for pressure vessel plates, alloy steel, double-normalized and tempered 9% Ni. Standard by ASTM International

ASTM A615/A615M-18E1 (2018) Standard specification for deformed and plain carbon-steel bars for concrete reinforcement. ASTM International. West Conshohocken, PA: www.astm.org

Batahgy AM, Gumenyuk A, Gook S, Rethmeier M (2018) Comparison between GTA and laser beam welding of 9% Ni steel for critical cryogenic applications. J Mater Process Tech 261:193–201
Bhattacharya S, Madabhushi S (2008) A critical review of methods for pile design in seismically liquefiable soils. Bull Earthq Eng 6:407–446
Booth E, Fenwick R (1994) Concrete structures in earthquake regions: design and analysis. Longman Scientific and Technical, Harlow
Boulanger RW, Kamai R, Ziotopoulou K (2014) Liquefaction induced strength loss and deformation: simulation and design. Bull Earthq Eng 12:1107–1128
Brandenberg SJ, Kwak DY, Zimmaro P, Bozorgnia, Y, Kramer, SL, Stewart, JP (2018) Next-Generation Liquefaction (NGL) case history database structure. Geotechnical earthquake engineering and soil dynamics V: liquefaction triggering, consequences, and mitigation. American Society of Civil Engineers Reston, VA
Brunelli A, De Silva F, Piro A, Parisi F, Sica S, Silvestri F, Cattari S (2021) Numerical simulation of the seismic response and soil–structure interaction for a monitored masonry school building damaged by the 2016 Central Italy earthquake. Bull Earthq Eng 19:1181–1211
Brunesi E, Nascimbene R, Parisi F, Augenti N (2015) Progressive collapse fragility of reinforced concrete framed structures through incremental dynamic analysis. Eng Struc 104:65–79
Buratti N, Tavano M (2014) Dynamic buckling and seismic fragility of anchored steel tanks by the added mass method. Earthq Eng Struct Dyn 43:1–21
Calderón M, Illing D, Veiga J (2016) Facilities for bunkering of liquefied natural gas in ports. Transportation Research Procedia 14:2431–2440
Carbonari S, Dezi F, Leoni G (2008) Seismic response of coupled wall-frame structures on pile foundations. Tailor made concrete structures: new solutions for our society. CRC Press, Florida, pp 1159–1161
Cavalieri F, Correia A, Crowley H, Pinho R (2020) Seismic fragility analysis of URM buildings founded on piles: influence of dynamic soil–structure interaction models. Bull Earthq Eng 18:4127–4156
Chaboche JL, Lemaitre J (1990) Mechanics of solid materials. Cambridge University Press
Christovasilis IP, Whittaker AS (2008) Seismic analysis of conventional and isolated LNG tanks using mechanical analogs. Earthq Spectra 24:599–616
Chun B, Jinn J, Lee J (2002) Modeling the Bauschinger effect for sheet metals, part I: theory. Int J Plast 18:571–595
Chung M, Kim J, Kim JK (2019) Feasibility study on the wide and long 9% Ni steel plate for use in the LNG storage inner tank shell. Steel Compos Struct 32:571–582
Dogangun A, Karaca Z, Durmus A, Sezen H (2009) Cause of damage and failures in silo structures. J Perform Constr Facil 23(2):65–71
Dash SR, Govindaraju L, Bhattacharya S (2009) A case study of damages of the Kandla Port and Customs Office tower supported on a mat–pile foundation in liquefied soils under the 2001 Bhuj earthquake. Soil Dyn Earthq Eng 29:333–346
Di Sarno L, Karagiannakis G (2020) On the seismic fragility of pipe rack—piping systems considering soil–structure interaction. Bull Earthq Eng 18(6):2723–2757
Dobry R, Abdoun T, O'rourke TD, Goh S (2003) Single piles in lateral spreads: field bending moment evaluation. J Geotech Geoenviron Eng 129:879–889
Driver G, Kulak L, Kennedy L, Elwi A (1998) Cyclic test of four-story steel plate shear wall. J Struct Eng 124:112–120
Dulinska JM, Jasinska D (2014) Performance of steel pipeline with concrete coating (modeled with concrete damage plasticity) under seismic wave passage. Appl Mech Mater 459:608–613
Elia G, Rouainia M (2016) Investigating the cyclic behaviour of clays using a kinematic hardening soil model. Soil Dyn Earthq Eng 88:399–411
Elwardany H, Seleemah A, Jankowski R, El-khoriby S (2019) Influence of soil–structure interaction on seismic pounding between steel frame buildings considering the effect of infill panels. Bull Earthq Eng 17:6165–6202
Eurocode-8 (2006) Design of structures for earthquake resistance, Part 4: silos, tanks and pipelines. European Committee for Standardization, Brussels
Eurocode (2008) Design of structures for earthquake resistance–Part 4: Silos, Tanks and Pipelines, vol 1. CEN national Members, Brussels
Gazetas G, Dobry R (1984) Horizontal response of piles in layered soils. J Geotech Eng 110(1):20–40
Gazetas G, Mylonakis G (1998) Seismic soil-structure interaction: new evidence and emerging issues. Geotech Spec Publ 1:119–1174
Genikomsou AS, Polak MA (2015) Finite element analysis of punching shear of concrete slabs using damaged plasticity model in ABAQUS. Eng Struct 98:38–48

George JK, Gross D, Jahed H, Roostaei A (2016) Fatigue life prediction of an automotive chassis system with combined hardening material model. Society of Automotive Engineers
Gičev V, Trifunac MD (2012) Energy dissipation by nonlinear soil strains during soil–structure interaction excited by SH pulse. Soil Dyn Earthq Eng 43:261–270
Gilbert RI, Warner RF (1978) Tension stiffening in reinforced concrete slabs. J Struct Div 104:1885–1900
Gingery JR, Elgamal A, Bray JD (2015) Response spectra at liquefaction sites during shallow crustal earthquakes. Earthq Spectra 31:2325–2349
Guzel Y (2019) Influence of input motion selection and soil variability on nonlinear ground response analyses. Doctoral dissertation, Newcastle University
Hawileh RA, Naser M, Zaidan W, Rasheed HA (2009) Modelling of insulated CFRP-strengthened reinforced concrete T-beam exposed to fire. Eng Struct 31(12):3072–3079
Haldar S, Babu GS (2010) Failure mechanisms of pile foundations in liquefiable soil: parametric study. Int J Geomech 10:74–84
Hardin BO, Drnevich VP (1972) Shear modulus and damping in soils: design equations and curves. J Soil Mech Found Div 98:667–692
Haroun M, Housner G (1981) Earthquake response of deformable liquid storage tanks. J Appl Mech 48:411–418
Hashiguchi K, Ueno M (2017) Elastoplastic constitutive equation of metals under cyclic loading. Int J Eng Sci 111:86–112
Hokmabadi AS, Leung E, So M, Yiu J (2019) Impact of soil-structure interaction on the seismic design of large LNG tanks. Transformation in geotechnical engineering - technology, digital and innovation, Hong Kong. HKIE Geotechnical Division Annual Seminar
Hokmabadi AS, Fatahi B (2016) Influence of foundation type on seismic performance of buildings considering soil–structure interaction. Int J Struct Stab Dyn 16:1550043
Hor B, Hyun Jee S, Song MJ, Kim DY (2017) Ground improvement using rigid inclusion for the foundation of LNG tanks. In: Proceeding of the 19th international conference on soil mechanics and geotechnical engineering. Seoul, Korea, pp 2907–2910
Housner GW (1957) Dynamic pressures on accelerated fluid containers. Bull Seismol Soc Am 47:15–35
Idriss IM, Boulanger RW (2008) Soil liquefaction during earthquakes, Earthquake Engineering Research Institute
Jiménez G, Dias D, Jenck O (2019) Effect of the soil–pile–structure interaction in seismic analysis: case of liquefiable soils. Acta Geotech 14:1509–1525
Kianoush M, Ghaemmaghami A (2011) The effect of earthquake frequency content on the seismic behavior of concrete rectangular liquid tanks using the finite element method incorporating soil–structure interaction. Eng Struct 33:2186–2200
Kmiecik P, Kamiński M (2011) Modelling of reinforced concrete structures and composite structures with concrete strength degradation taken into consideration. Arch Civil Mech Eng 11(3):623–636
Koo S, Han J, Marimuthu K, Lee H (2019) Determination of Chaboche combined hardening parameters with dual backstress for ratcheting evaluation of AISI 52100 bearing steel. Int J Fatigue 122:152–163
Kramer S (1996) Geotechnical earthquake engineering. Pearson Education India, London
Kupfer H, Hilsdorf HK, Rusch H (1969) Behavior of concrete under biaxial stresses. J Proceed 66(8):656–666
Lee RG, Dale BG (1998) Policy deployment: an examination of the theory. Int J Qual Reliab Manag. https://doi.org/10.1108/02656719810203659
Lee J, Fenves GL (1998) Plastic-damage model for cyclic loading of concrete structures. J Eng Mech 124(8):892–900
Lemaitre J, Chaboche JL (1994) Mechanics of solid materials. Cambridge University Press, Cambridge
Lombardi D, Bhattacharya S (2014) Modal analysis of pile-supported structures during seismic liquefaction. Earthq Eng Struct Dyn 43:119–138
Lubliner J (1990) Plasticity theory. Macmillan Publishing Company, New York
Lubliner J, Oliver J, Oller S, Oñate E (1989) A plastic-damage model for concrete. Int J Solids Struct 25:299–326
Lysmer J, Kuhlemeyer RL (1969) Finite dynamic model for infinite media. J Eng Mech Div 95:859–877
Malhotra PK, Wenk T, Wieland M (2000) Simple procedure for seismic analysis of liquid-storage tanks. Struct Eng Int 10:197–201
Masing G (1926) Eignespannungen and Verfestigung beim Messing. In:Proceeding 2nd international congress on applied mechanics, Zurich, Switzerland (in German)
Medina C, Aznárez JJ, Padrón LA, Maeso O (2013) Effects of soil–structure interaction on the dynamic properties and seismic response of piled structures. Soil Dyn Earthq Eng 53:160–175

Miglietta PC, Grasselli G, Bentz EC (2016) Finite/discrete element model of tension stiffening in GFRP reinforced concrete. Eng Struct 111:494–504
Mizuno D, Suzuki S, Fujita S, Hara N (2014) Corrosion monitoring and materials selection for automotive environments by using Atmospheric Corrosion Monitor (ACM) sensor. Corros Sci 83:217–225
Mucciacciaro M, Sica S (2018) Nonlinear soil and pile behaviour on kinematic bending response of flexible piles. Soil Dyn Earthq Eng 107:195–213
Murray A, Gilbert RI, Castel A (2018) A new approach to modelling tension stiffening in reinforced concrete. ACI Struct J 115:127–137
Mylonakis G, Gazetas G (2000) Seismic soil-structure interaction: beneficial or detrimental? J Earthq Eng 4:277–301
Nagashima M, Tsuchiya M, Asada M (2011) Reducing the economic risk of LNG tank construction under conditions of fluctuating resource prices. J Constr Eng Manag 137:382–391
Nateghi F, Yakhchalian M (2011) Seismic behavior of reinforced concrete silos considering granular material-structure interaction. Procedia Eng 14:3050–3058
Nayal R, Rasheed HA (2006) Tension stiffening model for concrete beams reinforced with steel and FRP bars. J Mater Civ Eng 18:831–841
Nikolaou S, Mylonakis G, Gazetas G, Tazoh T (2001) Kinematic pile bending during earthquakes: analysis and field measurements. Geotechnique 51(5):425–440
NZS1170.5 (2004) Structural design actions. Part 5: earthquake actions -New Zealand. New Zealand Standard. Wellington
NZSEE (2009) Seismic design of storage tanks: recommendations of a NZSEE study group on seismic design of storage tanks. New Zealand National Society for Earthquake Engineering, New Zealand
Oller S (2014) Numerical simulation of mechanical behaviour of composite materials. Springer, Cham
Padrón L, Aznarez J, Maeso O (2009) Dynamic structure–soil–structure interaction between nearby piled buildings under seismic excitation by BEM–FEM model. Soil Dyn Earthq Eng 29:1084–1096
PEER (2014) PEER ground motion database, *Pacific Earthquake Engineering Research Centre.* University of California, Berkeley, CA
Poulos HG (2017) Designing piles for seismic events. In: DFI-PFSF 2017 Conference. Melbourne p 28
Rasouli H, Fatahi B (2021) Geosynthetics reinforced interposed layer to protect structures on deep foundations against strike-slip fault rupture. Geotext Geomembr 49:722–736
Rostami R, Hytiris N, Bhattacharya S, Giblin M (2017) Seismic analysis of pile in liquefiable soil and plastic hinge. Geotech Res 4:203–213
Ruiz DP, Gutiérrez SG (2015) Finite element methodology for the evaluation of soil damping in LNG tanks supported on homogeneous elastic halfspace. Bull Earthq Eng 13:755–775
Saenz LP (1964) Discussion of" equation for the stress-strain curve of concrete" by Desayi and Krishnan. J Am Concr Inst 61:1229–1235
Sakr MA, Sleemah AA, Khalifa TM, Mansour WN (2019) Shear strengthening of reinforced concrete beams using prefabricated ultra-high-performance fiber reinforced concrete plates: experimental and numerical investigation. Struct Concr 20:1137–1153
Seed HB (1987) Design problems in soil liquefaction. J Geotech Eng 113(8):827–845
Seed HB, Wong RT, Idriss I, Tokimatsu K (1986) Moduli and damping factors for dynamic analyses of cohesionless soils. J Geotech Eng 112:1016–1032
Seismic response of ground-supported circular concrete tanks. PhD thesis, Ryerson University
Seismosoft (2016) SeismoMatch 2016 – A computer program for spectrum matching of earthquake records, available from http://www.seismosoft.com
Solakivi T, Laari S, Kiiski T, Töyli J, Ojala L (2019) How shipowners have adapted to sulphur regulations–Evidence from Finnish seaborne trade. Case Stud Transp Policy 7:338–345
Son IM, Kim JM (2019) Evaluation of soil-structure interaction responses of LNG storage tank subjected to vertical seismic excitation depending on foundation type. J Comput Struct Eng Inst Korea 32:367–374
Squarzoni P, Oller G, Hoeffel G, Pont-Lezica L, Rostaing P, Garel S (2014) Microglia modulate wiring of the embryonic forebrain. Cell Reports 8(5):1271–1279
Stewart JP, Seed RB, Fenves GL, Trifunac M (2000) Seismic soil-structure interaction in buildings. II: empirical findings. J Geotech Geoenviron Eng 126:668–671
Sun J, Cui L (2015) Seismic response for base isolation of storage tanks with soil-structure interaction. Phys Numer Simul Geotech Eng 18:64–68
Sun JI, Golesorkhi R, Seed HB (1988) Dynamic moduli and damping ratios for cohesive soils, Earthquake Engineering Research Centre, University of California Berkeley
Tahnat Y, Dwaikat M, Samaaneh M (2018) Effect of using CFRP wraps on the strength and ductility behaviors of exterior reinforced concrete joint. Compos Struct 201:721–739

Tajirian FF, Tabatabaie M, Rao P (2019) Soil-structure interaction analysis of a large diameter tank on piled foundations in liquefiable soil. In: Geo-Congress 2019: earthquake engineering and soil dynamics. American Society of Civil Engineers Reston, VA, pp 169–180

Tokimatsu K, Mizuno H, Kakurai M (1996) Building damage associated with geotechnical problems. Soils Found 36:219–234

Trifunic MD (2000) Discussion of "Seismic soil structure interaction in buildings. I: analytical methods", and "Seismic soil structure interaction in buildings. II: empirical findings." J Geotech Geoenviron Eng 7:668–672

Veletsos A, Tang Y (1987) Rocking response of liquid storage tanks. J Eng Mech 113:1774–1792

Vermeer PA (1984) De Borst R (1984) Non-associated plasticity for soils, concrete and rock. Heron 29(3):1984

Virella J, Godoy L, Suárez L (2006) Dynamic buckling of anchored steel tanks subjected to horizontal earthquake excitation. J Constr Steel Res 62:521–531

Wahalathantri BL, Thambiratnam D, Chan T, Fawzia S (2011) Material model for flexural crack simulation in reinforced concrete elements using ABAQUS. In: Proceedings of the first international conference on engineering, designing and developing the built environment for sustainable wellbeing. Queensland University of Technology

Willford M, Sturt R, Huang Y, Almufti I, Duan X (2010) Recent advances in nonlinear soil-structure interaction analysis using LS-DYNA. In: Proceedings of the NEA-SSI workshop pp 6–8

Yang Z (2000) Numerical modeling of earthquake site response including dilatation and liquefaction. PhD Dissertation, Department of Civil Engineering and Engineering Mechanics, Columbia University, New York

Youd TL, Carter BL (2005) Influence of soil softening and liquefaction on spectral acceleration. J Geotech Geoenviron Eng 131:811–825

Zakavi SJ, Nourbakhsh M (2014) The ratcheting behaviour of stainless-steel pressurized piping elbows subjected to dynamic out-of-plane moments. World J Mech 4:125–132

Zhai X, Zhao X, Wang Y (2019) Numerical modeling and dynamic response of 160,000-m 3 liquefied natural gas outer tank under aircraft impact. J Perform Constr Facil 33:04019039

Zhang R, Weng D, Ren X (2011) Seismic analysis of an LNG storage tank isolated by a multiple friction pendulum system. Earthq Eng Eng Vib 10:253–262

Zhang R, Jia J, Wang H, Guan Y (2018) Shock response analysis of a large LNG storage tank under blast loads. KSCE J Civ Eng 22:3419–3429

Zhang Y, Tang Y (2007) Characterizing the dynamics of soil organic carbon in grasslands on theQinghai-Tibetan Plateau. Sci China Series D Earth Sci 50(1):113–120

Zhu X (2019) Effect of plastic hardening models on fatigue life simulation of pipeline elbows under operating pressure and cyclic bending. J Press Vessel Technol 141(6):1–18. https://doi.org/10.1115/1.4044340

Zhuang H, Hu Z, Wang X, Chen G (2015) Seismic responses of a large underground structure in liquefied soils by FEM numerical modelling. Bull Earthq Eng 13:3645–3668

Ziegler H (1959) A modification of Prager's hardening rule. Q Appl Math 17:55–65

Zienkiewicz O, Emson C, Bettess P (1983) A novel boundary infinite element. Int J Numer Meth Eng 19:393–404

Zimmaro P, Ausilio E (2020) Numerical evaluation of natural periods and mode shapes of earth dams for probabilistic seismic hazard analysis applications. Geosciences 10:499

Zimmaro P, Nweke CC, Hernandez JL, Hudson KS, Hudson MB, Ahdi SK, Boggs ML, Davis CA, Goulet CA, Brandenberg SJ (2020) Liquefaction and related ground failure from july 2019 ridgecrest earthquake sequence. Bull Seismol Soc Am 110:1549–1566

Authors and Affiliations

Noor Sharari[1] · Behzad Fatahi[2] · Aslan Hokmabadi[3] · Ruoshi Xu[4]

✉ Behzad Fatahi
behzad.fatahi@uts.edu.au

[1] School of Civil and Environmental Engineering, University of Technology Sydney (UTS), Sydney, Australia

[2] School of Civil and Environmental Engineering, Faculty of Engineering and Information Technology, University of Technology Sydney (UTS), City Campus, Broadway, PO Box 123, Sydney, NSW 2007, Australia

[3] Arup, Sydney Office, Sydney, Australia

[4] BG&E Consulting Engineers, Sydney Office, Sydney, Australia